Relict topography within the Hangay Mountains in central Mongolia: Quantifying long-term exhumation and relief change in an old landscape

Kalin T. McDannell[a,b]*, Peter K. Zeitler[a], and Bruce D. Idleman[a]

[a]*Department of Earth & Environmental Sciences, Lehigh University, 1 W Packer Ave., Bethlehem, PA 18015, USA*

[b]*Natural Resources Canada, Geological Survey of Canada, 3303 33 St NW, Calgary, AB T2L 2A7*

Corresponding author: kalin.mcdannell@canada.ca

Key Points

- New bedrock and detrital apatite (U-Th)/He cooling ages were determined for the Hangay Mountains and central Mongolia
- Thermo-kinematic modeling suggests relief lowering in the Mesozoic with slow exhumation rates on the order of 10 m/My since the Cretaceous
- Coupled Pecube-Neighborhood Algorithm modeling is successfully applied in a slowly eroding setting

Abstract

The Hangay Mountains are a high-elevation, low-relief landscape within the greater Mongolian Plateau of central Asia. New bedrock apatite (U-Th)/He single-grain ages from the Hangay span ~70 to 200 Ma, with a mean of 122.7 ± 24.0 Ma (2σ). Detrital apatite samples from the Selenga and Orkhon Rivers, north of the mountains, yield dominant (U-Th)/He age populations of ~115 to 130 Ma, as well as an older population not seen in the Hangay granitic bedrock data. These low-temperature data record regional exhumation of central Mongolia in the Mesozoic followed by limited erosion of <1-2 km since the Jurassic-Cretaceous, ruling out rapid exhumation of this magnitude associated with any late Cenozoic uplift. Apatite (U-Th)/He age-elevation patterns suggest long-term thermal stability of the upper crust, and thermal model inversions require rapid, moderate relief lowering of a few hundred meters during late Mesozoic exhumation to produce the observed cooling ages in the Hangay region. Alpine cirques and intact moraines are indicative of more recent, climate-driven erosion in the higher peaks of the western Hangay. These data support the notion that in the absence of strong tectonic or climate forcing, erosion is

limited and remnant landscapes can persist over 10s-100s of millions of years in a state of disequilibrium.

Keywords: Thermochronology, (U-Th)/He, Hangay, Mongolia, landscape evolution, Pecube

1. Introduction

The topographic evolution of landscapes offers a top-down perspective on understanding mountain-belt development through time. In recent decades, we have begun to understand that deformation, erosional unroofing, and climate can be coupled in active settings and that their system dynamics inherently regulate landscape geometries, [e.g., *Molnar and England*, 1990; *Raymo and Ruddiman*, 1992; *Zeitler et al.*, 2001]. Studies of exhumation in active mountains have shown that orogenesis can take place quite rapidly at rates and durations consistent with plate convergence, and that surface processes can remove large relief rapidly [*Montgomery and Brandon*, 2002]. Conversely, ancient mountains and the records of their origins are often different from their modern counterparts, making the analysis of orogenic and topographic development a challenge.

Over orogenic timescales, the primary control on erosion and landscape evolution in active regions is tectonic uplift [e.g. *Koppes and Montgomery*, 2009]. In slowly eroding landscapes, where there is little tectonism, isostasy is the primary contributor to exhumation and under typical crustal and mantle density conditions reduction of surface topography requires significant erosion [e.g. *Braun and Robert*, 2005]. The overall density structure of the lithosphere, in turn, controls the magnitude and distribution of isostatic adjustment to erosion, with less buoyant lithosphere demonstrating an inhibited isostatic response [e.g. *Fischer*, 2002]. Post-orogenic topography has been found to survive over extended timescales through various surface process interactions including landslide-erosion feedbacks [*Egholm et al*., 2013], and when sediment mobilization shear stresses are low and fluvial systems are transport-limited [*Baldwin et al.*, 2003]. These phenomena allow topographic and geodynamic aberrations to persist over hundred million-year timescales, rather than disappear within tens of millions of years after tectonism ceases.

Clues to the exhumation and relief history of a landscape are held in the thermochronologic record of surface rocks across both short and long topographic wavelengths [*Braun*, 2002; *Mancktelow and Grasemann*, 1997; *Stuwe et al.*, 1994]. Topography affects the upper-crustal thermal structure, with the severity of the thermal disturbance decreasing with depth and proportionally with the topographic wavelength [*Braun*, 2002]. At long topographic wavelengths (10s-100s of km), isotherms conform to the broad shape of the topography and cooling ages become independent of elevation, whereas at very short wavelengths (≤10 km) low-temperature isotherms do not fully conform to topography. In steady-state topography, rocks that are exposed at peaks have traveled a greater distance after crossing closure-temperature isotherms and therefore a cooling age increase with elevation is expected and provides a direct estimate of the exhumation rate [*Braun*, 2002]. Sampling at short wavelengths across steep valleys can be used to directly estimate the mean exhumation rate when higher temperature systems are used or in regions characterized by slow exhumation. An observed positive age-elevation relationship (AER) becomes flattened with respect to steady-state topography if there has been relief growth, or steepened and even inverted if topographic relief has been reduced [*Braun*, 2002]. Therefore, short wavelength AERs are suitable for exhumation-rate estimation, while sampling long topographic wavelengths can provide estimates of relief change [*Braun and Robert*, 2005].

The Hangay Mountains of central Mongolia are high-elevation (>3500-4000 m), low-relief topography within the Asian continental interior. Broad, low-relief topographic surfaces that stand prominently above median continental base level are common features of continental interiors. How these apparently epeirogenic areas reach and maintain high elevations is puzzling because of their great distance from plate boundaries. Several studies suggest that the Hangay Mountains were uplifted recently in the mid-late Cenozoic [e.g. *Cunningham*, 2001; *Windley and Allen*, 1993; *Yanshin*, 1975] or rapidly within the past 5 Ma [*Yarmolyuk et al.,* 2008]. Questions remain about the exact timing of surface uplift and whether the current topography is a youthful feature. To test this, inferences about topographic change and the erosion history of the upper crust can be made from spatial patterns in low-temperature thermochronology data. Here, we explore the ability of the apatite (U-Th)/He thermochronometer to constrain long-term, long-wavelength exhumation and relief evolution in the Hangay Mountains, where there is a lack of penetrative deformation, limited mass transport, and the regional climate has become increasingly arid from the Jurassic through the Cenozoic [*Hendrix et al.*, 1992; *Caves et al.*, 2014; *Jolivet et al.*, 2015]. The elevated Hangay landscape itself thus shows no evidence for significant exhumation (more than 1-2 km) associated with any possible younger surface uplift, and likewise detrital age data show no evidence of such exhumation anywhere in the extensive Selenga River catchment. This study suggests that the topography in the Hangay region is not young, but a relict feature that has persisted since the late Mesozoic. This work is part of a multi-institutional collaboration to study the development of high topography in intracontinental settings and the geodynamic and biologic implications of surface uplift in central Mongolia, specifically, addressing lithosphere-asthenosphere character and dynamics, Asian climate change, and climatic-tectonic forcing of landscapes [*Ancuta*, 2017; *Carlson and Ionov*, 2014; *Caves et al*., 2014; *McDannell*, 2017; *Meltzer et al.*, 2012; *Meltzer et al.*, 2015; *Sahagian et al.,* 2016; *Smith et al.,* 2016; *Stachnik et al.,* 2014; *Wegmann et al*. 2014].

2. Regional setting and geologic history

The Hangay Mountains are a high-elevation region in the Asian continental interior and offer the unique opportunity to study an old landscape in a setting affected by recent tectonism (fig. 1). The Hangay Mountains sit within the Mongolian Plateau (2.6 million km^2) between the Siberian craton to the north and the Tarim and North China cratons to the south. The Hangay are also situated between the Altai Mountains (transpressional zone) and northern extensional zone of the Khövsgöl and Baikal rifts. The ranges in central Mongolia and southern Russia form the northernmost extent of the Central Asian Orogenic Belt (CAOB), which was a long-lived accretionary system, ca. 1000-250 Ma [*Windley et al.,* 2007]. The CAOB is composed of accretionary complexes including micro-continent blocks, volcanic arcs, back-arcs, and fore-arcs. This accretionary phase is believed to have lasted from Late Precambrian to Late Paleozoic time when terrane suturing and closure of the Mongol-Okhotsk Ocean was complete [*Kroner et al.*, 2007; *Lehmann et al.*, 2010]. The Mongol-Okhotsk Ocean was located between the Siberian and Mongolian (Amuria) blocks during Paleozoic-Mesozoic time and closed along a scissor-like suture in the eastern CAOB [*Tomurtogoo et al.,* 2005]. The exact timing of closure is debated, as the Late Jurassic-Early Cretaceous appears to represent a period of rapid Mongol-Okhotsk closure based on the apparent clockwise rotation of Siberia during collision with the North China block [*Cogné et al.,* 2005], while Late Triassic-Early Jurassic exhumation was driven by Qiangtang-Eurasia collision [*Gillespie et al.,* 2015]. *Yang et al.* [2015] assessed the Jurassic-Cretaceous transition and propose that a brief (ca. 10 Ma), but significant collision occurred in the Late Jurassic-Early Cretaceous driven by collision of Siberia with the Kolyma-Omolon (Russia-Mongolia) block. Subsequently, there was rapid transition to an escape tectonics setting driven by Lhasa Block collision and slab break-off. Strike-slip system development and gravitational collapse of the upper crust gave way to the continental-scale extensional setting in East Asia accommodating India-Asia collision [*Yin*, 2010]. Seismic analysis in the Tugrug Basin (Valley of Lakes region) also supports a rapid change from orogenic thickening to collapse in the Late Jurassic [*Johnson et al.,* 2015]. Thermochronologic data from the Kyrgyz Tian Shan and Siberian Altai-Sayan confirm regional cooling during the initial stages of the Mongol-Okhotsk orogeny and contemporaneous Lhasa collision at about 150 Ma, with orogenic collapse occurring afterwards around 100 Ma [*Glorie and De Grave*, 2016].

Mongolia is divided into two major geologic domains: a northern zone of Precambrian basement rocks and a southern zone of Paleozoic sedimentary and volcanic rock. The basement of the Hangay Dome is Archean to Early Proterozoic and is composed of metamorphic rocks unconformably overlain by Cambrian through Devonian (meta)sedimentary units. The crystalline and sedimentary rocks were intruded by Permian and Jurassic post-orogenic granitoids and underwent deformation during major Late Paleozoic compression [*Lehmann et al.*, 2010]. The granitoid massifs of the Hangay batholith yield zircon U-Pb crystallization ages of 260-242 Ma [*Yarmolyuk et al.*, 2008] while the Khentiyn batholith (abbrev. KM; fig. 1) is 220-200 Ma [*Yarmolyuk et al.*, 2001]. Formation of the Hangay batholith is believed to be related to magmatism associated with the Mongolian-Siberian craton collision [*Zorin*, 1999] or from post-orogenic intraplate magmatism [*Jahn et al.*, 2000].

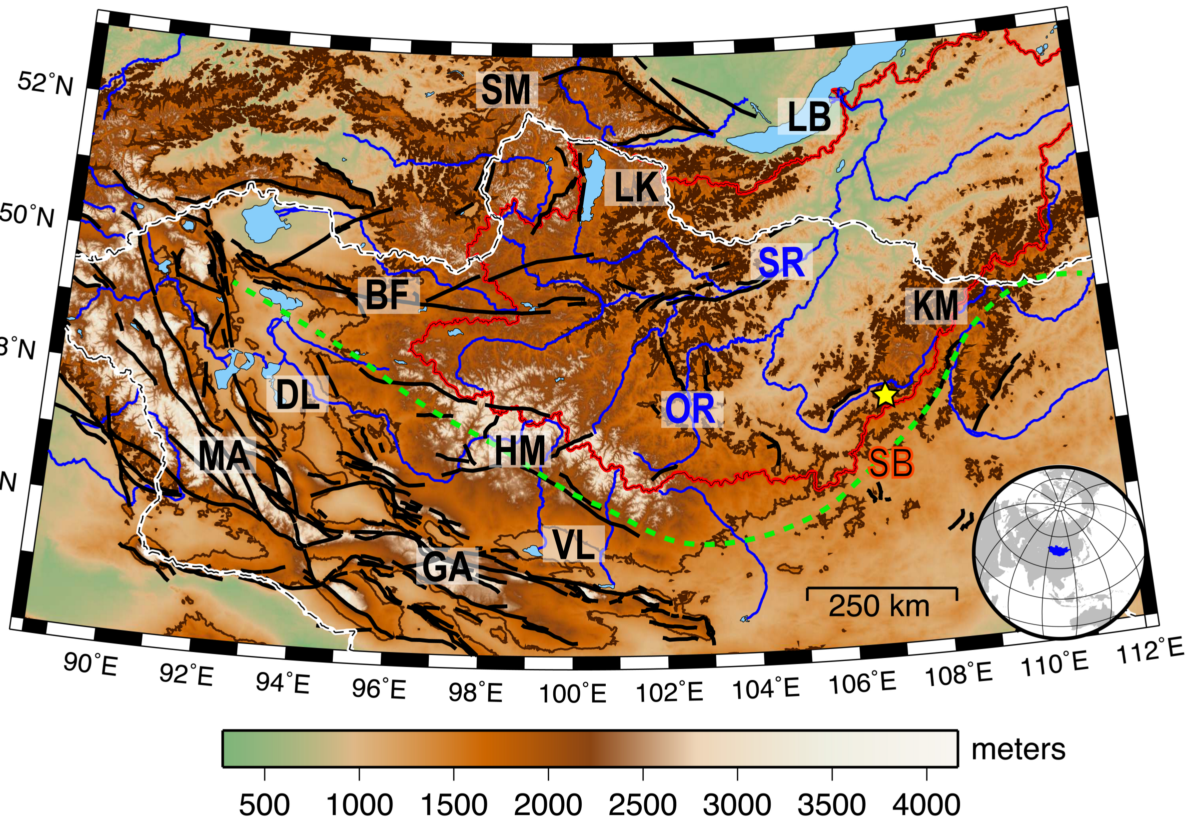

Figure 1: Regional map showing areas of high topography within Mongolia and southern Russia. The mean elevation in this view extent is 1500 ± 563 m and shows that the Hangay, Khövsgöl, Khentiyn, and Sayan Mountains (Russia) are a region of long-wavelength, high topography that has been dissected by the Selenga River network that drains the northern flank of the Hangay into Lake Baikal. Note that the deformation patterns vary regionally, i.e. the strong, large fault control in the Sayan versus the diffuse, smaller faults of the Hangay. The dark brown line denotes the 1500 m topographic contour. Regional fault systems are also shown; the sinistral Bulnai (BF) is the major strike-slip fault north of the Hangay separating the Sayan/Khövsgöl from the Hangay. The Mongolian (MA) and Gobi Altai (GA) ranges south of the Hangay are within a major transpressional fault system. The Siberian craton margin begins just north of the Sayan Mountains in the < 500 m elevation region (green) near the Mongolia-Russia border and Lake Baikal at ~53ºN latitude. Blue lines are major permanent streams draining higher elevations and the red line denotes the Selenga River system drainage divide. Heavy white line is Mongolian political border. Green dashed line is approximate Mongol-Okhotsk Ocean suture from *Van der Voo et al.* [2015]. Yellow star is Ulaanbaatar, the capital city. (MA=Mongolian Altai; GA=Gobi Altai; DL=Depression of Lakes; VL=Valley of Lakes; HM=Hangay Mountains; LK=Lake Khövsgöl; KM=Khentiyn Mountains; SM=Sayan Mountains; OR=Orkhon River; SR=Selenga River; LB=Lake Baikal; SB=Selenga basin). Major towns in Hangay region shown on figure 2.

Gravity data along with seismic tomography and mantle xenolith information have allowed interpretation of the lithospheric structure below the Hangay-Khövsgöl region [*Ionov et al.*, 1998; *Petit et al.*, 2002; *Zorin et al.*, 1990]. The lithosphere thinner in Mongolia relative to the Siberian craton, and cratons to the south. Gravity anomalies are associated with localized lithospheric flexure from the current compressional stress regime [*Petit et al.,* 2002]. Deep ($\geq$100 km) anomalous buoyant lithosphere is causing a long-wavelength, low-amplitude negative gravity signal with regional uplift of ~400 m, crustal velocity dampening, and a low-density lower crust-upper mantle beneath the Hangay, that results in a high amplitude gravity residual and localized uplift of ~700 m [*Petit et al.*, 2002; *Petit et al.,* 2008]. The uplifted high topography of the Mongolian Plateau (and central Mongolia) has mainly been described as a distal expression of the India-Asia collision [*Molnar and Tapponnier*, 1975; *Vassallo et al.*, 2007]. However, other proposed uplift mechanisms include, Pacific plate subduction [*Yanovskaya and Kozhevnikov*, 2003], localized mantle plume activity [*Windley and Allen*, 1993], asthenospheric upwelling and support [*Cunningham*, 2001; *Petit et al.*, 2008; *Tiberi et al.*, 2008; *Chen et al.*, 2015], delamination of the lithospheric mantle [*Hunt et al.*, 2012], and thickened crust resulting from mafic underplating [*Stosch et al.*, 1995; *Petit et al.*, 2002].

2.1 Regional thermochronology

During the Middle to Late Mesozoic, parts of central Asia were characterized by a topographic planation surface [e.g. *Cunningham*, 2001; *Hetzel et al.,* 2011; *Jolivet,* 2017]. The Hangay Mountains, Sayan-Baikal ranges, and the Altai systems all show preserved Jurassic through Paleogene peneplain surfaces at elevations ranging from a few hundred meters to up to 4000 m [*Cunningham*, 2001; *Jolivet et al.*, 2007; *Vassallo et al.*, 2007; *De Grave et al.*, 2009; *Jolivet et* *al.*, 2013; *West et al.*, 2013; *Glorie and De Grave*, 2016]. In the Hangay Mountains, Valley of Lakes, and Gobi Altai, rocks from relict erosional surfaces have Jurassic-Early Cretaceous apatite fission-track (AFT) ages [*Jolivet et al.*, 2007; *Vassallo et al.*, 2007]. The similarity in AFT ages at peak summits in the Mongolian-Gobi Altai, Hangay, and the adjoining Valley of Lakes piedmont suggests that cooling below ca. 110°C occurred at roughly the same time across this region and these surfaces were at the same paleo-depth (see fig. 8; *Jolivet et al.* [2007]).

Central Mongolia also shares similarities with mountains in neighboring southern Russia. The mountains around Lake Baikal record AFT ages between ~140-100 Ma and experienced rapid cooling in the Early Cretaceous, indicated by thermal-history modeling of AFT length distributions [*van der Beek et al.*, 1996; *Jolivet et al.*, 2009]. AFT ages from the Siberian Altai and Western Sayan of Russia are Jurassic to Cretaceous in age [*De Grave et al.*, 2009; *Jolivet et al.*, 2013; *Glorie and De Grave*, 2016]. Apatite fission-track thermal models for the Sayan suggest long-term erosion rates of 17.5 m/My, while ^{10}Be cosmogenic data suggest short-term (10^5 years) rates of 12-20 m/My [*Jolivet et al.*, 2013]. ^{10}Be cosmogenic data from basins in the eastern Hangay also show erosion rates between 12-20 m/My [*Hopkins*, 2012]. Short and long-term rates are similar and at first-order imply an extended period of nearly constant, slow erosion since the Mesozoic across Mongolia and southern Russia.

2.3 Hangay geomorphology

Stratigraphy and basin analysis of the Tian Shan Mountains (see supplement for location) shows that the aforementioned Late Mesozoic tectonic reorganization and surface uplift shut off the monsoon system in central Asia, and aridification occurred through the Late Jurassic [*Hendrix et* *al.*, 1992; *Jolivet et al.*, 2015]. This region of central Asia has been arid through the end Mesozoic and Cenozoic and much of the aridification is attributed to the uplift of the Tibetan Plateau and corresponding intraplate mountain belts extending to the north towards the Siberian craton [*Molnar et al.*, 2010]. Observed shifts in regional isotopic aridity signatures support the timing of Hangay surface uplift to be at least as old as Oligocene, and Late Miocene for the Altai range [*Caves et al.*, 2014].

The ages of tilted sediments and volcanic rocks exposed on the flanks of the Hangay also support Oligocene doming and surface uplift of the Hangay, which is also broadly coincident with the initiation of regional volcanic activity [*Devyatkin*, 1975; *Cunningham*, 2001]. Basalt vesicle paleo-altimetry shows the surface of the Hangay may have been modestly uplifted by up to 1 km over the past ~10 Ma [*Sahagian et al.*, 2016]. Stratigraphic relationships between basalt flows and granitic bedrock document the existence of ~700 m of local paleo-relief in central Mongolia [*Smith et al.*, 2016], and this pre-existing topography is similar to the modern topography. Basalt $^{40}Ar/^{39}Ar$ ages constrain the minimum age of the Hangay landscape to the Oligocene [*Ancuta*, 2017], while ^{14}C dating indicates that material in lacustrine deposits overlying basalt flows near Tariat (fig. 2 for location) are as young as ~5 Kya [*Logachev et al.*, 1982].

The central Mongolian fluvial network comprises alluvial streams with high sediment loads and limited transport ability due to many factors, including prolonged high aridity and spatially variable fluvial network integration. The Selenga River has a large drainage network (447,000 km^2) that sources the entire northern flank of the Hangay and most of central Mongolia and flows north into Lake Baikal, contributing a large volume of the lake water supply. The Orkhon

River is one of the major Selenga tributaries flowing out of the glaciated eastern Hangay (fig. 1 and fig. 2). The river network has modestly eroded most of the northern Hangay since minor late Cenozoic surface uplift. *West et al.* [2013] recognized two major river profile knickpoints near the northern and southern Hangay margins at ~2500 m elevation and estimate that up to 1-1.5 km of total erosion (relative to the reconstructed pre-incision/peneplain surface) have occurred below these knickpoints and in other areas in the eastern Hangay.

Geomorphic observations coupled with $^{40}Ar/^{39}Ar$ dated whole-rock basalt stratigraphy [*Ancuta*, 2017] allow us to calculate minimum incision rates in the Hangay region (fig. 2). The Orkhon River headwaters show rates of ~20 m/My through the late Pliocene to Holocene, while Orkhon headwater tributaries show late Pliocene through Holocene rates of ~30-60 m/My. At the Orkhon River waterfall (Ulaan Tsutgalan) basalts are ~700 Ka in age and yield incision rates of ~35 m/My. The northern flank of the Hangay shows rates of ~10 m/My in 13-14 Ma basalts exposed along the Ikh Tamir River, a tributary of the Orkhon. The Chuluut River valley, to the west, shows variable incision rates of 10-23 m/My over the past ca. 8-10 Ma. Basalt incision rates are similar to the aforementioned cosmogenic erosion rates in adjacent drainages and those estimated at Egiin Davaa in the central Hangay of ~25-77 m/My over the past 9 Ma [*Smith et al.*, 2016]. Basalt damming of river valleys in the past few million years establish that isolated flows caused accelerated incision (fig. 2), but overall these rates are comparable to those seen in old orogens such as the Appalachians [e.g. *Matmon et al.*, 2003; *McKeon et al.*, 2014].

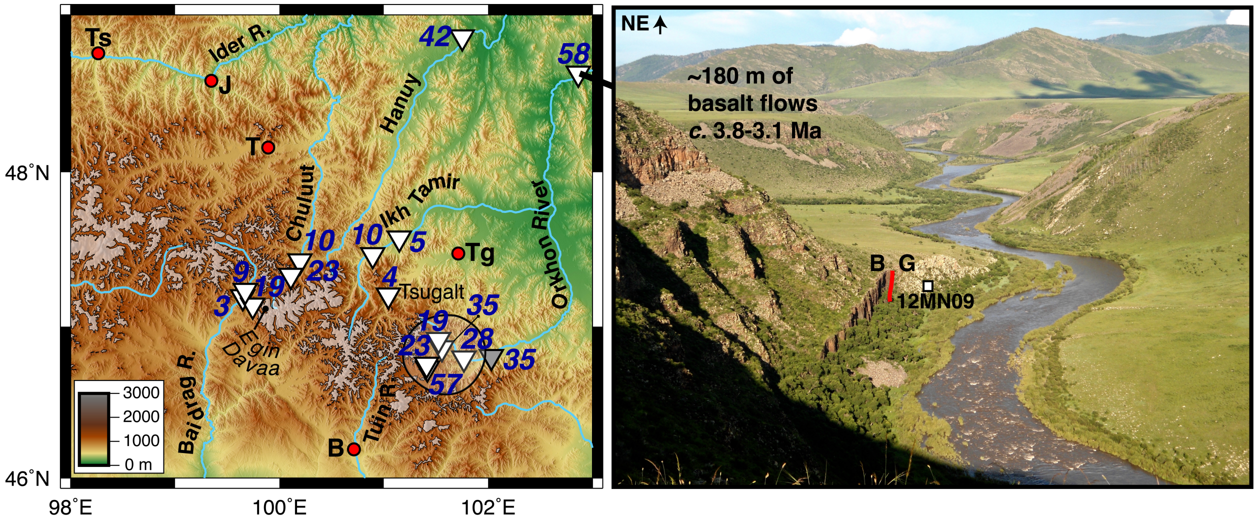

Figure 2: The eastern Hangay Mountains and major rivers (blue lines) with high elevation areas glaciated in the LGM shown in gray. River incision estimates at locations (triangles) from basalt age data presented in *Ancuta* [2017]. Numbers shown are in incision rates in m/My. Circled area in the southeast is the headwaters of the Orkhon River. Gray triangle is the Orkhon waterfall location (Ulaan Tsutgalan). Photo on the right shows a canyon location along the Orkhon River, at lower elevations in the Selenga River basin, where the higher incision rates (~58 m/My) are due to local basalt flow damming (~180 m total thickness) over the past 3 m.y. Red dots mark major towns in the area. B = Bayankhongor; J = Jargalant; T = Tariat; Tg = Tsetserleg; Ts = Tosontsengal. Photo: The contact between granitic basement and the basalt flows is shown by the red line in the photo. Apatite (U-Th)/He sample 12MN09 is from the granite bedrock [mean (U-Th)/He age of ~325 Ma].

The Hangay Mountains were glaciated in the Pleistocene during the Last Glacial Maximum [*Lehmkuhl et al.*, 2004]. Evidence for this exists in the form of well-defined cirques and preserved moraine deposits. There are currently no permanent alpine glaciers in the Hangay, but cryoplanation features, patterned ground, and other glacial features exist at high elevations and advocate a more recent climate-driven erosion signal in the past few million years. Cryoplanation terraces are typically just below relict planation surfaces at high elevations (fig. 3) [*West et al.,* 2013]. *Lehmkuhl* [1998] estimates the equilibrium line altitude (ELA) of the last glacial maximum (LGM) to be at ~2700-2800 m elevation. Current ELA estimates are ~3700 m [*Lehmkuhl and Lang,* 2001], which is ~1000 m higher than the Pleistocene ELA and at fairly high elevations relative to the highest peaks of the Hangay (~4000 m), thereby limiting the potential for modern glaciation. The highest peaks show evidence of cryoplanation terraces down to 3100-3300 m elevation, while most glacial processes below 2600 m in the Hangay are limited in extent and mainly restricted to frost shattering of bedrock [*Lehmkuhl and Lang,* 2001]. Presumably, glaciation in the western Hangay near Otgontenger (fig. 3) has recently created more dramatic topographic relief, which is almost twice the relief observed in lower elevations near the Selenga River headwaters (see suppl. figure S2).

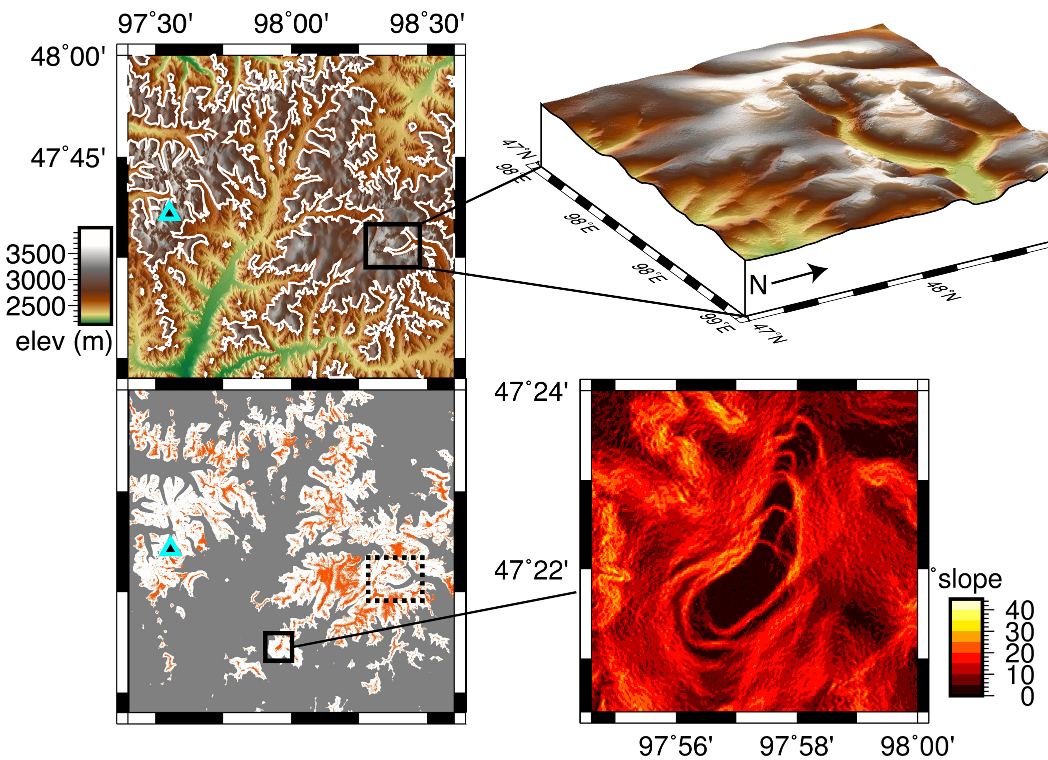

Figure 3: Imagery showing the regional topography near the highest Hangay peak, Otgontenger Uul (triangle). The areas outlined in white are the ELA for the LGM at 2800 m elevation. The image below is of the same area as above but showing elevations >2800 m (gray area is <2800 m) and areas with slopes ≤5° (orange). Enlarged digital elevation model (DEM) inset (top right, looking 240° at 20° inclination) shows example of high elevation relict planation surface and associated cryoplanation features east of Otgontenger. Bottom panel is a slope map of another such area to the south with a flat, relict surface and cryoplanation terraces. See *West et al.,* [2013] for other examples.

3. Methodology

3.1 Apatite (U-Th)/He thermochronology

Granitic bedrock and detrital sediments were collected for apatite (U-Th)/He (AHe) analysis throughout central Mongolia. Igneous bedrock samples went through standard procedures for rock crushing, sieving (<250 microns), Frantz magnetic splitting, and heavy-liquid separation using lithium polytungstate and methylene iodide. Unbroken, symmetric apatite grains without visible inclusions were selected under a high-power petrographic microscope at 250-300X magnification. Samples were digitally photographed in order to record their 3D morphology for determination of alpha-correction factors using a cylindrical geometry. Grains were then placed in small Nb tubes whose ends were crimped and loaded into the extraction system in the Lehigh University noble gas laboratory for analysis following conventional methodology (see below) or underwent continuous ramped heating treatment [*Idleman et al.*, 2018; *McDannell et al.*, 2018]. ^{4}He and the ^{3}He spike were measured using a Balzers bakeable quadrupole mass spectrometer designed for UHV operation, fitted with both Faraday and electron-multiplier detectors. For helium extraction, a double-vacuum resistance furnace was used for heating, and an all-metal sample dropper permits multiple samples to be loaded for sequential analysis in the resistance furnace. Helium evolved from heated samples was purified in an all-metal extraction line pumped by an ion pump during routine operation as well as a 70 l/s turbo-molecular pump with a small rotary backing pump used during bake-out. An SAES GP50 getter in the extraction line removes active gases, while a smaller SAES getter in the mass spectrometer volume is used to minimize hydrogen loads. Reservoirs containing a ^{3}He spike and a ^{4}He/^{3}He standard are attached to the line behind all-metal pipettes while two temperature-stabilized capacitance manometers provide the precise, accurate pressure measurements needed for spike preparation (the extraction line ^{4}He blank is $1x10^{-16}$ moles or less). ^{4}He was measured by isotope dilution, using a ^{3}He spike, and also by manometric peak-height comparison against a mass-discrimination standard.

Generally these approaches agree to better than 1% and the dual calibrations provide an internal crosscheck. Over periods spanning the analysis of sample batches, the $^{4}He/^{3}He$ ratio for the standard was precise to within 0.3%, with a value of about 0.795 (the true $^{4}He/^{3}He$ ratio of standard is 1.000). For the current spike preparation, the size of a typical spike is 4 x 10^{-13} moles. Following helium extraction, U, Th, and Sm measurements were obtained from the University of Arizona in the laboratory operated by Dr. Peter Reiners, where samples were dissolved, spiked, and analyzed using isotope-dilution ICP-MS [*Reiners and Nicolescu*, 2006]. U, Th, and Sm were measured on the same aliquots of apatite that were used for He determinations, eliminating any uncertainties contributed by weighing errors and sample heterogeneity. A mean age of 31.85 ± 0.24 Ma (2 SE, n=78) for the Durango apatite age standard has been acquired over repeated experiments in the Lehigh noble gas laboratory. *McDowell et al.* [2005] obtained a direct $^{40}Ar/^{39}Ar$ reference age of 31.13 ± 0.42 (2 SE) for Durango apatite.

3.2 Detrital apatite (U-Th)/He modeling

3.2.1 Inference of detrital cooling age distribution components

The BayesMixQt program allows Bayesian inference of probability distributions regarding the number of component age distributions from a set of individual mineral cooling ages and their associated errors under Gaussian or Skew assumptions [*Jasra et al.,* 2006]. More simply, it allows identification of discrete age components (mixture modeling) in a larger age distribution and is well suited for the heterogeneity often encountered in detrital age datasets. The modeling infers the proportion of each individual distribution that contributes to the total distribution as well as the parameters that define each distribution (i.e. mean and standard deviation). The approach implements Reversible Jump Markov chain Monte Carlo methods that employ an iterative sampling scheme and allow changes in the problem-space dimensionality (i.e. component distributions). This approach requires defining prior and proposal distributions for the dataset and allows a "burn-in" phase for exploratory sampling of the model space, which is used to infer the component distribution parameters (i.e. post-burn-in phase). Refer to *Jasra et al.* [2006] for a more complete overview of mixture modeling.

3.2.2 Catchment-averaged erosion rates and topographic relief histories from detrital data

The age distribution of detrital mineral cooling ages provides a proxy for the erosional history of mountain catchments [e.g. *Brewer et al.*, 2003]. The range of cooling ages can also provide information about erosion timing and magnitude. The detrital age range for a catchment is proportional to the time needed to erode the total relief in the source region [*Brewer et al.*, 2003; *Ruhl and Hodges*, 2005], while narrow or broad age spread is interpreted as rapid or slow erosion rate, respectively [*Stock and Montgomery*, 1996]. Assuming uniform erosion and a positive trend AER, the observed elevation distribution in a catchment should produce a predicted age probability density function (PDF) that matches the hypsometry (fig. 4) [*Brewer et al.*, 2003; *Ruhl and Hodges*, 2005; *Stock et al.*, 2006]. If there is non-uniform erosion in a catchment then the predicted age PDF will be out of phase with the hypsometric curve or have multiple peaks corresponding to the areas of the catchment that are being more heavily eroded (fig. 4) [*Stock et al.*, 2006; *Ehlers et al.*, 2015]. Equations (1-3) after *Ruhl and Hodges* [2005] describes this relationship:

$$PDF = \frac{1}{\sigma t_m \sqrt{2\pi}} \exp\left[-\frac{1}{2}\left(\frac{t - t_m}{\sigma t_m}\right)^2\right] \qquad (1)$$

Where t is the PDF of the age, t_m is the measured age with the analytical uncertainty, σ. The synoptic probability function (SPDF) is the summation of all individual grain PDFs multiplied by the reciprocal of the number of detrital grains normalized to unity.

(2)

$$SPDF = \frac{1}{n}\sum_{i=1}^{n} PDF\ (i)$$

The shape of the SPDF should mimic the hypsometric curve if bedrock erosion scales with surface area and the cooling ages accurately reflect the eroded sediment signal. The cumulative synoptic probability function (CSPDF) represents the probability that the age takes on a value less than or equal to t, the PDF of the cooling age. The CSPDFs are normalized hypsometric curves of elevation, z^*, and cooling age, t^*, and assuming uniform erosion, should overlap.

(3)

$$CSPDF = \sum_{i=0}^{t} SPDF\ (j)$$

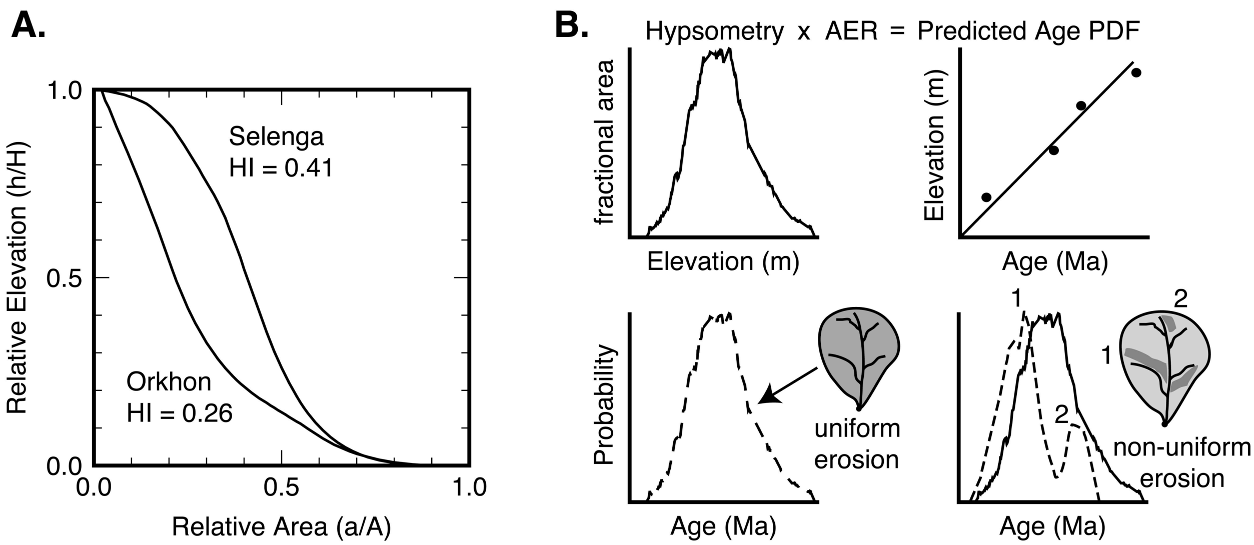

Figure 4: **(A)** Hypsometry of the Selenga and Orkhon River sub-catchments sampled for detrital AHe (see figure 5 for locations; section 5 for discussion). **(B)** Schematic diagram illustrating the relationship between detrital thermochronometer data and the hypsometry of a catchment given an assumed positive age-elevation relationship where cooling ages should match the hypsometric curve if erosion is uniform, i.e. all points on the topography produce cooling ages that correspond to the basin AER. If there is non-uniform erosion, then the elevations on the landscape contributing sediments will affect the SPDF curve accordingly, modified after *Stock et al.* [2006].

3.3 Methods: Coupled Pecube-Neighborhood Algorithm modeling

Pecube [*Braun*, 2003] is a finite-element thermo-kinematic model that solves the 3D heat transport equation in a crustal block with the allowance of a time-variable surface boundary condition (topography) including the effects of isostasy. Pecube predicts thermochronometric ages for crustal scenarios involving erosional or fault-driven exhumation. In our Pecube inversions we adopt spatially constant material properties for the crust (table 1) and a sub-region of central Mongolia is modeled as a single uplifting block, as the entire Hangay and thermochronology dataset coverage are too large to model efficiently (see section 5.4 for location and discussion). A SRTM digital elevation model of central Mongolia resampled to 1 km resolution was used as the topographic input. The conventional volume diffusion model of *Farley* [2000] has typically been used for AHe age prediction, and in the case of grains with low (<20-30 ppm) effective uranium (eU) content [*Flowers et al.*, 2009], and/or rapid cooling this model is satisfactory and does not require more sophisticated age prediction models that account for compositional or radiation damage effects [e.g. *Flowers et al*., 2009; *Gautheron et al*., 2009]. Since radiation damage tends to suppress partial He loss, the closure temperature varies in proportion to the eU and cooling rate, thus contributing to the observed apatite cooling age dispersion commonly seen in slowly cooled settings. The *Flowers et al.* [2009] radiation damage model was incorporated for age prediction within Pecube for modeling of our Mongolia data. Pecube and previous applications are reviewed thoroughly in *Braun et al.* [2012]. Here we summarize some of the main features relevant to this study.

During a Pecube model inversion, the use of a two-step *Neighborhood Algorithm* (NA) inverse approach is employed, where during the sampling stage the multi-dimensional prior model space is efficiently sampled to find the best-fitting parameter combinations that produce the lowest user-defined misfit between observed and predicted data [*Sambridge*, 1999a]. The appraisal stage then allows robust measures of parameter resolution to be extracted in the form of Bayesian marginal posterior probability density functions (PPDF) during resampling of the model ensemble [*Sambridge*, 1999b]. During the sampling stage an initial model ensemble is randomly generated using the prior parameter range (assumed uniform distribution) of the Pecube variables. The misfit is assessed and Voronoi cells are created about nearest neighbor models that are subdivided after successive iterations as the algorithm focuses on regions of lower misfit by resampling the previous iteration. We employed an objective function or χ^2 misfit of the form:

(2)

$$\mu = \sum_{i=1}^{n} \left(\frac{m_i - o_i}{\sigma_i}\right)^2$$

Where μ is the misfit value, n is the number of data, and for each datapoint i, o_i is the observed age, m_i is the model age, and σ_i the observed age error. During the NA appraisal stage the entire sampling-stage ensemble is resampled to gain Bayesian estimates of parameter values and assess the resolution of the lowest misfit via the Likelihood function, *L,* to assess the likelihood of different model predictions, given in the simplified form as:

(3)

$$L = \exp(-\tfrac{1}{2}\chi^2)$$

In the case of χ^2 misfit, the simplified form of the *log (L)* is equal to -0.5 multiplied by the misfit value [*Glotzbach et al.*, 2011]. The motivation for examining individual model misfit during the appraisal stage is that the lowest misfit can be misleading, for example, the lowest misfit may be identified for an individual parameter, but in the multi-dimensional case the overall misfit is a combination of several parameters where the identified best fit may have a single parameter value that is associated with a large misfit due to trade-offs in multi-dimensional space. Posterior probability accounts for this, because although it is a function of all parameters, it may be integrated over one or more parameters to examine the best estimate of that parameter independent of the others in the form of a 1-D marginal PPDF curve. Parameters plotted as 2-D marginal PPDFs examine potential correlative tradeoffs between different parameters. In the case of a purely Gaussian PPDF the results are interpreted as a mean/mode value at the peak maximum, and in the case of a skewed PPDF, the mode is at the maximum probability peak of the PPDF curve.

The sampling stage has typically been performed iteratively but here we use the MPI-enabled parallelized version of the code that does away with 'formal iterations' and instead of the misfit being assessed at the end of an iteration, it is continuously assessed during the inversion, leading to more efficient algorithm performance [*Rickwood and Sambridge*, 2006]. The number of iterations, the number of models in each iteration step, and the resampling rate all control the NA-sampler stage and influence the NA search. Although there are no specific rules for these configurations, a lower resampling rate allows faster convergence, albeit with the danger of prematurely converging on local minima, while a greater resampling rate allows more thorough exploration of the ensemble space but is slower to converge. Generally, inversions with a greater number of free parameters require a larger number of iterations to converge on the best fitting parameter combination.

The relief amplitude, *R,* in Pecube is fairly simplistic as it assumes the planform geometry of the topography does not change, only the amplitude varies, i.e. valleys and ridges do not migrate laterally [*Valla et al.,* 2010; *van der Beek et al.*, 2010]. This assumption is justified in equilibrated landscapes with low erosion. *R* is defined as the ratio between the relief amplitude (Δh_i) when rocks passed through the closure isotherms and the modern-day relief amplitude (Δh_0). Where: (4)

$$R = \frac{\Delta h_i}{\Delta h_0}$$

According to the model definition, where $R = 1$ is the modern topography, when $R = 0$ the initial topography is a plateau (no relief); for $R < 1$ relief has grown from the past to present; while for

$R > 1$ relief has decreased from past to present [*Beucher et al.,* 2012; *Valla et al.,* 2010]. The erosional (or relief change) timescale, τ, is a function that describes how relief evolves through time, either in an exponential or linear fashion, where 0 is a linear change in relief in the model between time steps (equation 5). When values are highly positive, relief change will take place rapidly at the model onset, and if τ is highly negative the relief change will take place close to present day [*Beucher et al.*, 2012].

$$\Delta h_t = \Delta h_0 + \left[(R-1)\Delta h_0 \frac{1-e^{\left(-\frac{t\tau}{t_{f2}}\right)}}{1-e^{\left(-\frac{\tau}{t_f}\right)}} \right] \tag{5}$$

Pecube-NA inversions have been applied successfully to high-relief regions that have experienced relatively high exhumation rates and recent relief development such as the European Alps [*van der Beek et al.*, 2010] and Southern Alps [*Herman et al.,* 2010]. There has been varying success in applying this approach to determine relief histories accurately and difficulties are attributed to incomplete sampling of topography at multiple wavelengths, and the insensitivity of low-temperature thermochronometers to rapid topographic change or high exhumation rates [e.g. *Valla et al.*, 2010; *Reverman et al.,* 2012]. *Valla et al.* [2010] explored the efficacy of estimating denudation rates and relief histories using the Pecube-NA inversion and the resolving power of the AFT and AHe low-temperature thermochronometers. They suggest that settings where relief development is approximately two to three times higher than background exhumation rates, or where background exhumation rates are generally low, as being more suitable for relief-change investigations. Central Mongolia is a setting where the latter is likely to be true throughout the latest Mesozoic and Cenozoic.

4. Apatite (U-Th)/He thermochronology results

4.1 Bedrock (U-Th)/He data

Granitoid bedrock samples were collected across the Hangay and areas to the north (fig. 5; suppl. table S1 for data). We dated 106 single-crystal aliquots of apatite (44 bedrock samples) and also report 12 multi-grain aliquots (5 bedrock samples) dated at Lehigh University during pilot Mongolia sampling presented in *Landman* [2007]. For mean age calculations, bedrock ages that were older than reported Hangay U-Pb ages of ~250 Ma were discarded as outliers. However, there is a lack of age control for granitoids to the north, and those found in the Altai in southwest Mongolia have older zircon U-Pb populations spanning 289-317 Ma and 350-398 Ma [*Cai et al.*, 2015], considerably older than the ~240-250 Ma granites in the Hangay. This allows for the possibility that there are older granites to the north that exhumed prior to those in the Hangay.

Age dispersion in slowly-cooled settings is a common issue [e.g., *Fitzgerald et al.*, 2006; *McDannell et al.,* 2018] that is often attributed to factors such as fluid and mineral inclusions [e.g. *Farley*, 2000], U-Th zonation [e.g. *Farley et al.,* 2011], and radiation damage effects [e.g. *Shuster et al.,* 2006]. We ran a number of replicate grains for each sample in order to identify any dispersion, and it does occur in a few samples. The convention is to analyze 2-5 replicate single grains for each sample; however, robust averaging methods are difficult to justify for small sample sizes less than 10 grains due to the effects of age dispersion and outlier treatment [e.g. *Vermeesch*, 2010]. Additionally, because factors such as U content, radiation damage, and grain size control kinetic properties and He retentivity [*Farley*, 2000; *Shuster et al.*, 2006], each grain from the same rock is in effect a separate thermochronometer, so statistical averaging is not always warranted. We report arithmetic mean ages only for the purpose of an overview of regional age patterns. Mean ages are not used in thermal modeling (see later sections), as it is a requirement to model single grains because each analyzed grain is unique in its kinetic properties and slow cooling amplifies these kinetic effects.

Single-grain ages replicate well within the central Hangay and cluster around ~100-120 Ma at various elevations with a few exceptions, while data outside the Hangay show greater variation and generally older ages (fig. 5). The cooling ages from the north flank of the range are marginally younger than elsewhere in the higher elevations (<100 Ma), which coincides with the focus of modern erosion and precipitation leading to peak height asymmetry in the Hangay [*West et al.*, 2013]. This regional cooling age pattern is similar to that of the Dabie Shan in China [*Reiners et al.*, 2003] where significant age differences exist between the range core and flanks, with a progressive younging of cooling ages toward the mountain interior. Modeling of these data required a twofold decrease of topographic relief over the past ~100 m.y. to produce observed age patterns [*Braun and Robert*, 2005].

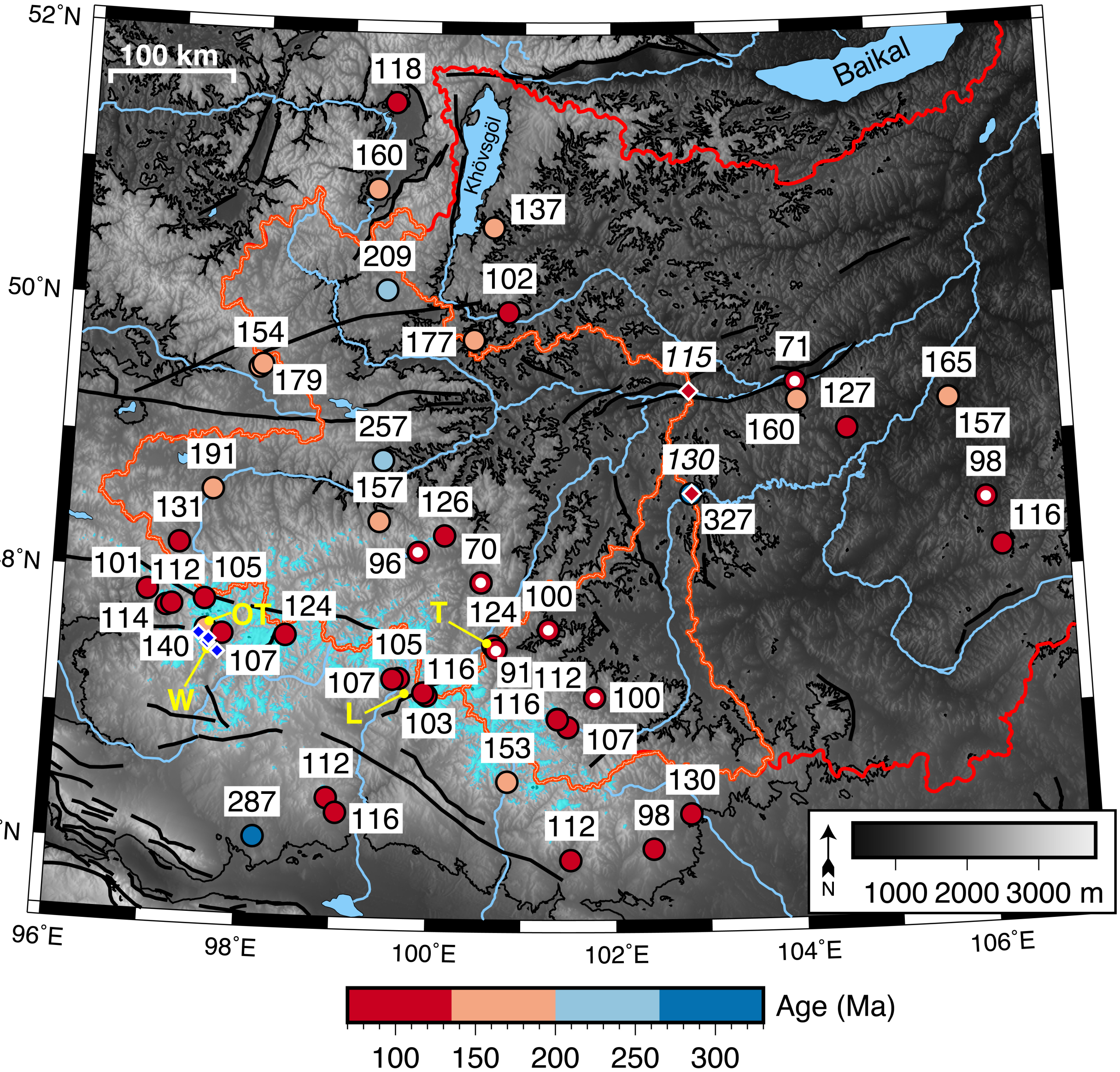

Figure 5: Granitic-bedrock mean AHe ages across the Hangay Mountains and north-central Mongolia colored by age. The majority of cooling ages in the Hangay are ca. 100-120 Ma, with a slightly younger grouping <100 Ma on the north flank (red/white center). Off the Hangay, ages are similar, albeit with greater scatter and an older component greater than ca. 120 Ma. Detrital sample locations are shown as diamonds (mean age in italics). The red line shows the Selenga watershed and sub-catchments with respect to detrital samples for the Selenga and Orkhon are the orange lines. Points tagged in yellow are AHe/AFT transect (W) of *West et al.* [2013] shown in blue diamonds, transect (L) of *Landman* [2007] near Egiin Davaa, and transect (T) discussed with figures 7 and 8. OT = Otgontenger Uul. Grayscale 90 m DEM with 1700 m contour to mark higher elevations above the regional background and onset of 'regional knickpoint elevation zone' discussed in text and with fig. 7. Glaciated high elevations areas shown in cyan blue, derived from the ELA during the LGM from *Lehmkuhl* [1998]. Major faults from *Tomurtogoo* [1999] geologic map of Mongolia shown by heavy black lines. See supplement for full age dataset.

4.2 Detrital (U-Th)/He data

The lower reaches of the Orkhon and Selenga Rivers were sampled to survey regional detrital apatite cooling ages (suppl. table S2 for data). The corresponding watersheds of the sampled locations are shown in figure 5. The motivation for detrital dating was to establish the age distribution that may be expected from bedrock ages, and to assess any dominant subsets. There was also an added motivation to determine if younger detrital ages were expressed that were missed by bedrock sampling. The Selenga and Orkhon Rivers (fig. 6) show similar age distributions with dominant peaks at ~115-120 Ma for the Selenga and a broad peak centered at ~130 Ma for the Orkhon (this central value is likely controlled by the low number of data).

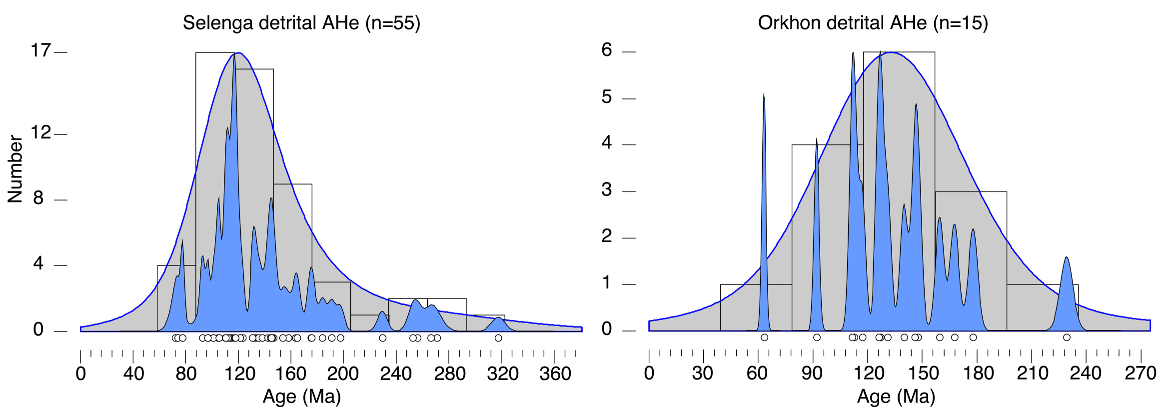

Figure 6: Selenga and Orkhon River detrital apatite (U-Th)/He cooling age populations shown by kernel density estimator (KDE) (smooth, gray envelope) and probability density functions (PDF) (shaded blue) from DensityPlotter [*Vermeesch*, 2012] using a Gaussian kernel and adaptive bandwidth (varied based on local data density). White dots show individual grain ages for the datasets. The y-axis is number of grains.

5. Modeling and interpretations

5.1 Detrital apatite (U-Th)/He modeling

Inference of the probability distribution of the number of detrital cooling age components was performed via BayesMixQt using Reversible Jump Markov-Chain Monte Carlo methods [*Jasra et al.*, 2006]. There are two major age components identified in the Selenga River sample with an expected model mean of 124 ± 29 Ma, representing 83% of the detrital population and an older component at 227 ± 51 Ma, representing 17% of the population (200,000 iterations, post burn-in). The Orkhon sample has very few grains and is less resolved, but mixture modeling reveals a single component maximum posterior peak at 131 ± 29 Ma, showing overall agreement between both rivers. The Selenga detrital population contains a few dates that may reflect the end of CAOB orogenic exhumation, while the majority of grains are from the last major exhumation event in the early Cretaceous during Mongol-Okhotsk suturing. The notable outcome from the detrital dating is that the area supplying sediment to these two locations contains an older age component that is not reflected in the Hangay bedrock samples, implying that the older ages are potentially coming from bedrock in the lower reaches of the catchments or that older cooling ages are sourced from glacially-eroded relict surfaces.

The hypsometry of the Selenga and Orkhon catchments relative to the detrital sample locations are quite different (fig 4). Both drainage basins have been glaciated (fig. 5), but the glaciation is limited in extent to only the highest elevations, compared to the overall basin areas. Based on the shape of the hypsometric integral, the Orkhon basin would be "mature or old," with the majority of the catchment area at low elevations, while the Selenga would represent a younger stage of development [*Strahler*, 1952]. Nevertheless, caution is required during interpretation because the influence of tectonics or fluvial/glacial processes, along with basin size and tectonic activity can render basin hypsometry non-unique [*Brocklehurst and Whipple*, 2004].

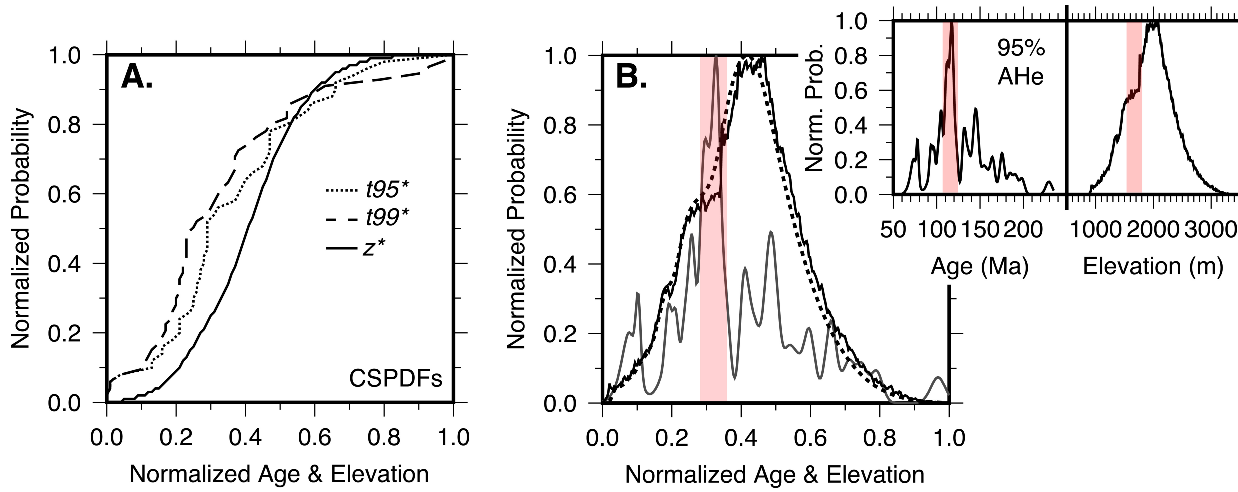

Figure 7: **(A)** Normalized CSPDF curves of Selenga detrital ages (dashed lines, t*) and catchment elevations (solid line, z*) for the Selenga River, using 95% and 99% of the detrital dataset, after *Ruhl and Hodges* [2005]. **(B)** SPDF curves for normalized age (gray) and elevation (solid black line) distributions with inset age and elevations (upper right). Dashed line in (B) is the 'ideal' age SPDF obtained from inverting the observed age SPDF and hypsometric curves with respect to the regional AER from the northern Hangay (figure 5, transect labelled T). Small inset panels show ages for 95% of the detrital AHe dataset and the elevations in the Selenga sub-catchment and red shading shows the dominant mismatch in age/elevation from the ideal age SPDF, see text for details.

Figure 7 show plots of detrital cooling age PDFs from equation 1-3 after *Ruhl and Hodges* [2005]. To minimize the mismatch between normalized age and elevation curves due to uncertainty in cooling ages, both the 95% and 99% detrital SPDF were used to construct the *t** CSPDFs, which effectively removes a small component of the older age signal. The $CSPDF_{t*}$ curves are slightly offset from the $CSPDF_{z*}$ curve for the Selenga basin, suggesting non-uniform erosion and a preferential erosional zone at elevations between ~1600-1800 m in the northern Hangay landscape. *Whipp et al.* [2009] showed through 3D thermal modeling that an increase in relief causes a shift in the detrital age population towards older ages relative to steady-state relief, whereas a relief decrease would have an opposite trend. This is directly linked to the higher or lower effective denudation rate between each respective relief change scenario. The mismatch/shift towards younger ages in fig. 7B may be in line with the relief-decrease age shift of *Whipp et al*. [2009]. The Orkhon basin curves are not shown due to the limited number of dated grains.

We solve for the expected uniform erosion AER by dividing the observed detrital PDF by the hypsometry to obtain the slope of the ideal AER to match the hypsometry. This produces a predicted slope of 0.068 that is then compared to a bedrock age-elevation transect on the north flank of the Hangay in the Selenga sub-catchment (see fig. 5 for location), which yields a slope of 0.060 (dashed predicted age SPDF curve in fig. 7B). Another short bedrock age transect from the valley floor to the Orkhon headwaters cirque yields a slope of 0.059. Near Otgontenger Uul, the highest elevation peak in the glaciated interior of the Hangay, age-elevation transects are shown in figure 8 using our data and cooling ages from *West et al.* [2013], *Jolivet et al.* [2007], and *Landman* [2007]. Here, AER slopes are greater but still similar to the predicted and measured AER slopes in the Selenga basin. The slight mismatch in the PDF curves could be due to:

1) Sampling bias or outlier ages: The Selenga basin sources not only the Hangay, but lower elevations to the north that have a slightly older, albeit scattered, cooling age signal and therefore are eroding more slowly than the Hangay. Bias could be introduced from the dating process itself or be naturally occurring if a higher proportion of ‘younger’ Hangay sediments were being supplied to the lower reaches of the basin. Naturally occurring bias may be a reflection of alpine cirque cutting and higher erosion along steeper slopes of the Hangay. There is also the possibility of sampling other Mesozoic-Paleozoic bedrock and older, recycled sediments. If this were the case, it would seem that this is a fairly small proportion of dated grains. Alternatively, some of these slowly-cooled apatites could be

cooling age outliers that are skewing the age PDF; this situation is apparent in the 95% $CSPDF_{t*}$ curve, which more closely matches the hypsometry by removing only the oldest ages from the detrital population.

2) Detrital under-sampling: The Selenga CSPDFs are reminiscent of those presented by *Ruhl and Hodges* [2005] for the Marsyandi trunk stream in Nepal where there is also departure of the $CSPDF_{t*}$ from the elevation range. This was attributed to sediments not capturing the full bedrock age signal in a very large catchment. This could very well be the case here as well, since the sampled Selenga catchment is >95000 km^2 in size.

3) The 'spike' in the measured detrital age PDF is the only main point of deviation between the PDFs and occurs at a large step in the hypsometric curve, which roughly aligns with the shift from the background low-lying elevations in the deeper basin to the elevated landscape of the Hangay. This shift likely signifies a regional, preferential cooling age 'erosional zone' that is the current focus of incision at the crossover into higher elevations of the Hangay where more sediment of the primary detrital peak is being sourced. In line with this, the mismatch between hypsometry and the age CSPDF may also signify a change in erosion rate at ~120-130 Ma, which agrees to first-order with the *West et al.* [2013] apatite fission-track AER (fig. 8).

The large spread in our observed detrital ages suggests that erosion has been slow, of low magnitude, and operative over a prolonged period since the Mesozoic. In a simplistic 1-D case where lateral advection is ignored, an erosion rate over the time represented by the detrital population can be calculated by simply dividing the total catchment relief by the cooling age range, which in this case is quite long, >150 Ma. Long-term slow erosion and low modern relief suggest that the shallow isotherms have conformed to the topography, and a simple 1-D technique is adequate for erosion rate estimation [*Whipp et al.*, 2009]. To reduce the influence of potential outlier ages, only cooling ages falling within 95% of the detrital population mean were used. The detrital apatites from the Selenga catchment that source the majority of the western Hangay and northern Mongolia show a time-integrated erosion rate ($\dot{E}$) ≈ 17 m/My, which decreases to ~10 m/My if the entire detrital dataset is used. This is in agreement with the independently derived basalt incision rates for the late Cenozoic and previous thermochronologic and cosmogenic estimates for the region cited in section 2, all in accordance with a long-term history of slow erosional exhumation.

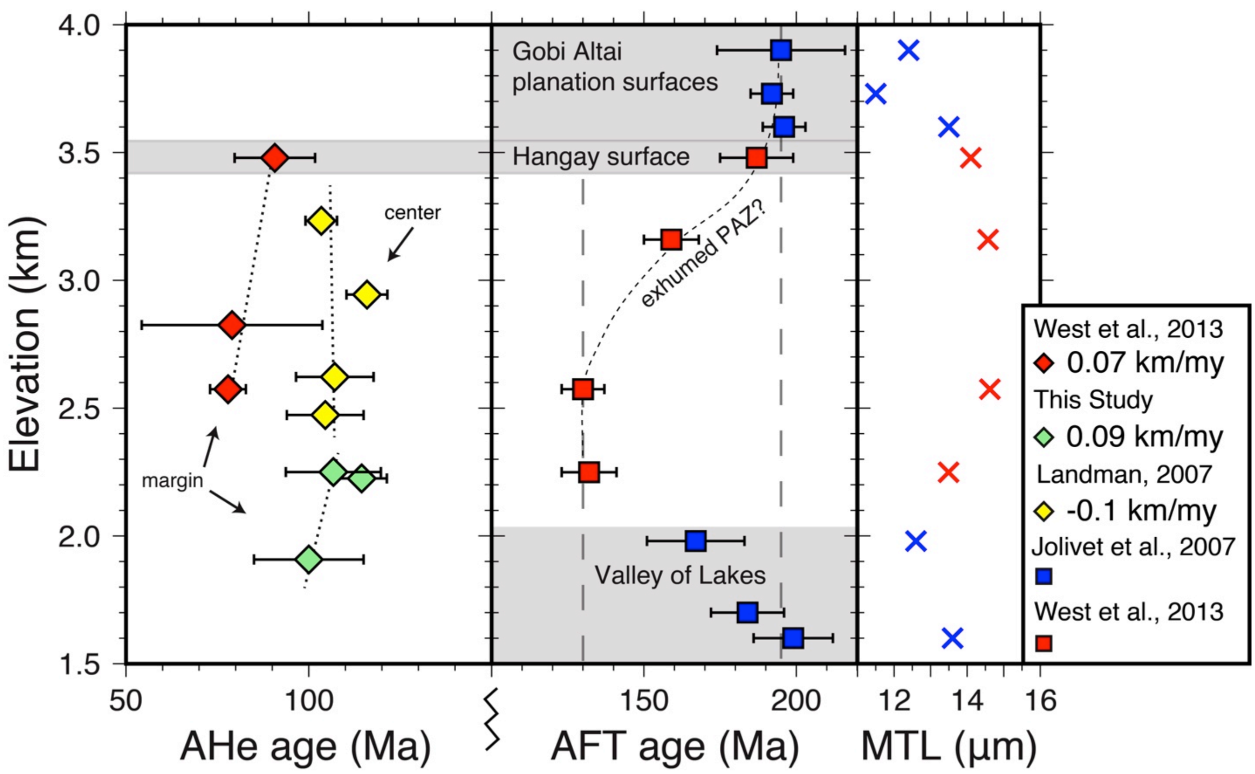

Figure 8: Apatite AERs (left panel) from the western Hangay near Otgontenger (highest peak; figs. 3 and 4) incorporating a short transect from this study and from *West et al.* [2013] and *Landman* [2007] datasets (see fig. 5 for transect locations). Positive AERs suggest valley-scale topographic wavelengths do not affect low-T isotherms. Right panels show AFT and mean fission-track lengths (MTL) for *Jolivet et al.* [2007] and *West et al.* [2013] datasets. Planation surfaces in the Gobi Altai, Valley of Lakes, and W. Hangay (gray) are all similar in age suggesting regionally coincident exhumation and that highest

elevations are preserved remnants from an older event. *West et al.* AFT transect suggests the period between ~180-130 Ma being governed by a moderate exhumation rate.

Conversely, the detrital cooling age range and the AER can be used to estimate the paleo-relief of a catchment [*Stock and Montgomery*, 1996]. On the large scale in the slowly-eroding Hangay, isotherms would presumably now be parallel to the surface, and assuming horizontal isotherms, the exposed bedrock ages divided by the modern relief yields the change in cooling age with elevation. By the same token, the detrital age range divided by the AER provides estimates of the paleo-relief. The apatite fission-track AER of *West et al.* [2013] spans 46.34 ± 0.24 Ma over 1.23 ± 0.01 km of modern elevation (using 10 m elevation errors from 90 m DEM) in the western Hangay. Using the 95% spread about the mean Selenga detrital age approximates catchment paleo-relief of 3.39 ± 0.1 km, or a 0.79 ± 0.1 km decrease in relief in the time represented by the sub-basin detrital dataset.

Our detrital age sample population is too small to allow a definitive assessment of landscape change, although assumptions of widespread steady-state erosion in the Hangay are invalidated. It is reasonable to suspect that the landscape has experienced variable, finite erosion since the Cretaceous that has been more focused in certain areas of the landscape. The continued existence of the remnant planation surfaces across the Hangay is further evidence that an erosional steady state has yet to be reached. The recent surface uplift has potentially complicated the erosional history and provided a "regional knickpoint" at the uplifted Hangay margins for focused incision, which is supported by knickpoints in river profiles at elevations of ~2000-2500 meters [*West et al.*, 2013]. The eastern Hangay and Orkhon watersheds contain the majority of Cenozoic valley-filling basalts that have dammed valleys and locally disrupted the fluvial system by resetting base level in the last ca. 10-15 Ma. Our geomorphic observations, detrital data, and the findings of *West et al.* [2013] agree and support modest glaciation, recent surface uplift, and modern precipitation gradients as the cause of localized erosional variability in this setting. Our detrital AHe ages also suggest areas of the Hangay landscape near ~1600-1800 m elevation are the focus of erosional unroofing.

5.2 Pecube-NA thermo-kinematic modeling

We are interested in not only the long-term exhumation of the region but also the relief evolution through time. We performed modeling analogous to the Dabie Shan study of *Braun and Robert* [2005] to ascertain the topographic and thermal histories necessary to produce the observed AHe dataset for central Mongolia using Pecube.

5.3 Inversion resolution tests

As a first step, we ran a Pecube-NA sensitivity test inversion to evaluate if exhumation rates and relief could be adequately constrained for the Hangay. Values for erosional timescale (τ), relief amplitude (R), and exhumation rate timing (E-timing) were set and run through a forward Pecube model to produce synthetic AHe and AFT cooling ages (with 6% and 10% errors, 2σ). These synthetic ages were then used as input in a Pecube inversion (results shown in table 2) to determine if the true values could be recovered. The sensitivity test recovered the true parameter values and the overall misfit was very good, however the assigned synthetic-age errors were larger than the observed analytical errors on our data, and so were more permissive of good fits.

We then tested whether moderate relief change in a slow exhumation setting is adequately modeled using Pecube-NA (fig. 9). We set background exhumation rates from exhumation phase

#1, E_1, from 180-90 Ma at 0.1 km/My and a second slower phase, E_2, from 90-0 Ma at 0.03 km/My. The relief amplitude, *R*, is set to 0.5 (50% of modern relief) at the model start, and the erosional timescale, τ, to 750 Ma. These variables are fixed and a Pecube forward model predicts model AHe and AFT cooling ages output at the same locations as observed data applying 6% AHe and 10% AFT age errors. The model ages and respective errors are then supplied back into two NA inversions, one where the relief amplitude is the only free parameter varying between 0-2, and the other with τ, *R*, and E-timing set free. This second test is to examine the ability to identify the true parameter values and any tradeoff effects. The second resolution test initially allowed E_1 and E_2 as free parameters but during initial tests the "true" rates were quickly identified, therefore during later inversions the background exhumation rates were fixed.

The relief amplitude-only sensitivity test inversion (fig. 9A) was set to run for >6000 total models with 96 models in an initial iteration and 96 models in each subsequent iteration with a 96% resampling rate. Convergence on the true value of $R = 0.5$ was found within a few hundred models but the algorithm was allowed to run to ~850 models before the run was stopped due to adequate convergence. This result verifies that in the case of well-known thermo-kinematic parameters and high quality thermochronometric data, relief growth in a post-orogenic setting can be resolved accurately to within <2% in a short number of iterations, in this example the best 50 models resulted in an $R = 0.49 \pm 0.02$ (1σ).

The sensitivity test inversion for τ, *R*, and E-timing was run with an initial and subsequent pool of 112 models over 75 iterations with a 68% resampling rate for a total of 8504 models (fig. 9B-F). The lowest misfit values matched the true values very accurately, suggesting the absence of synthetic noise in the resolution test. The model appraisal shows that relief amplitude was well resolved with a mode and standard deviation of 0.57 ± 0.23 for *R* and E-timing mean of 90.2 ± 5.5 Ma. The erosional timescale showed considerable scatter but was within one standard deviation of the true value. Trade-offs between parameter combinations can be noted in figure 9C. Under fixed exhumation rates, relief amplitude decreases non-linearly as the relief-change timescale increases, while the timing of exhumation rate change is positively correlated with both relief amplitude and relief-change timescale.

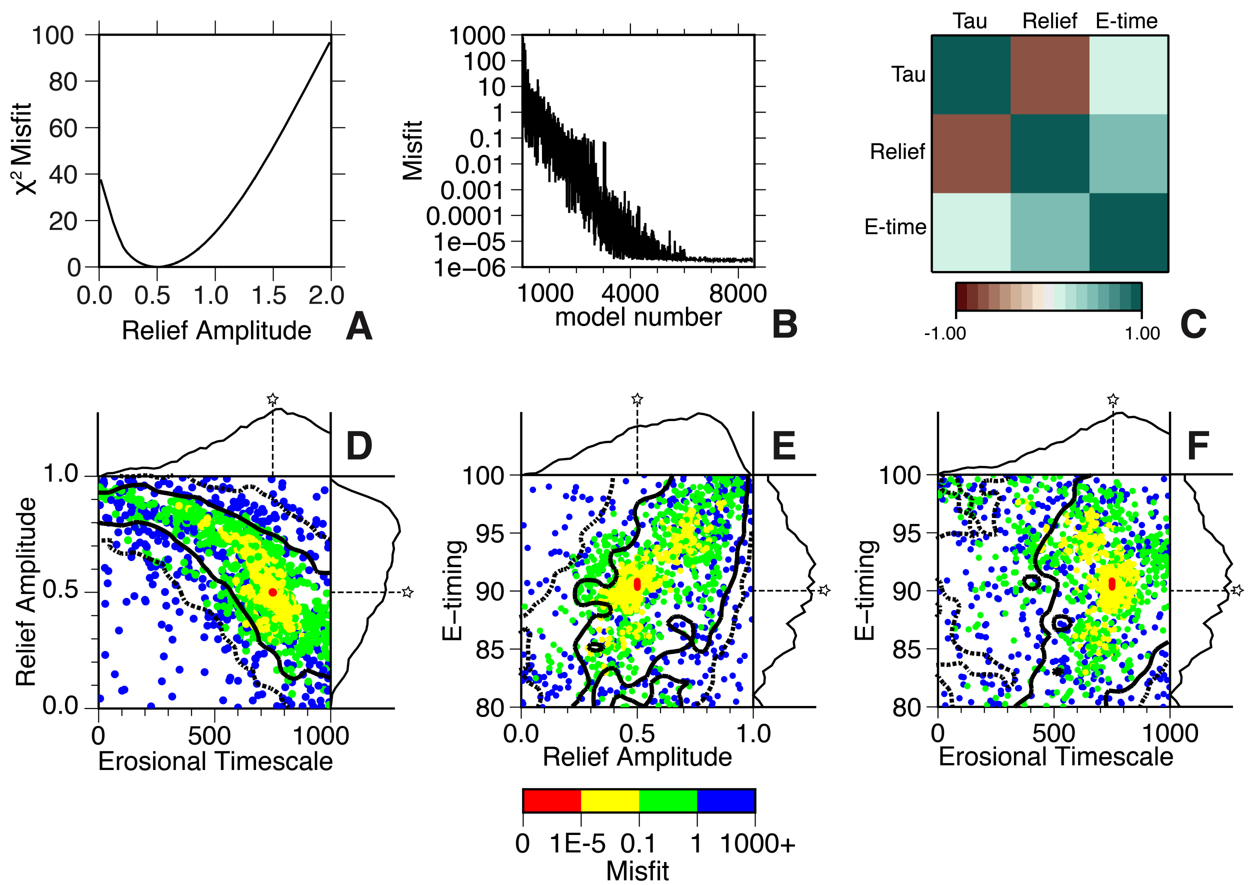

Figure 9: Pecube-NA sensitivity test of variables controlling relief to assess the ability to resolve relief change in this type of slow exhumation setting. For tests, a two-phase exhumation scenario was used with fixed rates of 100 m/My and 30 m/My. **(A)** Sensitivity test for *relief amplitude-only* showing least-squares misfit and relief amplitude between 0 (no relief) to 2 (two times modern relief) with a defined misfit minima at the true value of 0.5X the modern relief in the Hangay. **(B)** Misfit evolution over the sensitivity test inversion where τ, R, and E-timing are allowed free, exhibiting optimal convergence after >6000 models. **(C)** Correlation matrix for the free inversion parameters using NA-plot [*Sambridge*, 1999b]. Values approaching (-1)+1 show greater (anti)-correlation while values near 0 show no

relationship or dependence. Erosional timescale and relief amplitude are highly anti-correlated, while both the exhumation rate change timing and relief amplitude have a slight positive correlation with erosional timescale. These trends can also be seen in the PPDFs in panels D to F. **(D-F)** Scatter plots showing misfit between τ, *R* and E-timing, the 2-D PPDF 1σ (solid) and 2σ (dashed) contours shown as overlays and the corresponding 1-D marginal PPDF curves for each parameter on the corresponding axes. In each case the star marks both the 'true parameter value' and in this case, the respective lowest misfit of the 1-D PPDF, which in this synthetic example is also the mean or modal value.

5.4 Pecube-NA model inversion results

Following the sensitivity tests, we then applied Pecube-NA modeling to learn about the landscape evolution in Mongolia. The AHe thermochronologic data suggest low background exhumation rates have been sustained over the past ~100 m.y., so here we test resolving power of the Pecube-NA model to estimate timing and magnitude of long-term exhumation rates and paleo-relief histories using a modest data subset in the western Hangay. We use representative values for crustal thickness, basal temperature, etc. for Mongolia (table 1) and our data input consists of replicate single grain AHe cooling ages and those reported in *West et al.,* [2013]. Figures 10 and 11 and table 2 show inversion results. We ran ~10,000 models for each inversion with a resampling rate between ~60-70% to obtain adequate convergence and sampling of the model space.

We report results for two inversions that simulate the last 150 Ma in the western Hangay (see figs. 12 and 13 for location). One inversion (run 1-TSW) held the major exhumation phase timing fixed from 150-130 Ma, which was derived from the modeled AFT thermal history of *West et al.* [2013]. The optimal relief history and basal temperature (geothermal gradient) were investigated in this run. A second inversion attempt allowed the end of the exhumation phase to be a free parameter (run 1-C). The second inversion with the unrestricted exhumation phase was mainly for comparative purposes, as delayed or prolonged exhumation may have been possible in different parts of Mongolia during the end of the Mongol-Okhotsk orogeny in the Jurassic through the Cretaceous.

Table 1: Model parameters used in Pecube-NA inversions

Fixed Parameter	Value	Units	Reference
Model initiation	150	Myr	
Basal Moho temperature, *Tb*	850	°C	*Ionov et al.,* 1998; *Ancuta*, 2017
Volumetric heat production, *H*	0.7	μW m^{-3}	*Lysak and Dorofeeva*, 2003
Radiogenic heat production, *A*	8	°C Myr^{-1}	
Thermal diffusivity, *κ*	25	km^2 Myr^{-1}	
Specific heat capacity, *Cp*	800	J kg^{-1} K^{-1}	
Surface Temperature, *Ts*	0	°C	
Atmospheric lapse rate	0	°C km^{-1}	
Crust/Mantle density, *ρc/ρm*	2800/3300	kg m^{-3}	
Crustal Thickness, *Zc*	49	km	*Stachnik et al.,* 2014
Effective elastic thickness, *Te*	6.1	km	*Bayasgalan et al.,* 2005
Model domain	80 x 60	km	
1 km grid resolution	0.00833	degrees	
Vertical node spacing	1	km	

Table 1: Fixed model parameters used in Pecube inversions to calculate the isostatic and thermal response to varying relief.

Table 2: Pecube-NA inversion results

SENSITIVITY TEST			
Inversion Parameter	**True value**	**Inversion Results**	**Mean ± SD**
Erosional timescale (Myr), τ	750	**750.1** (0:1000)	608 ± 260
Relief amplitude, *R*	0.5	**0.50** (0:1)	0.57 ± 0.23
Exhumation change timing (Myr), E-timing	90	**90.4** (100:80)	90.2 ± 5.5
Exhumation rate 1 (km Myr^{-1}), E_1	0.1	-	-
Exhumation rate 2 (km Myr^{-1}), E_2	0.03	-	-
Number of models	8512		
Lowest misfit, μ	1.8E-06		
Misfit type	χ^2		
Free parameters	3		
Models/Iterations	112/75		
Resample rate	68%		

FULL INVERSIONS	INVERSION 1		INVERSION 2	
Inversion Parameter	**Run 1-TSW**	**Mean ± SD**	**Run 1-C**	**Mean ± SD**
τ	**930** (0:1000)	890.6 ± 110	**482** (0:1000)	491.7 ± 43
R	**1.58** (0:2)	1.62 ± 0.08	**1.24** (0:2)	1.20 ± 0.07
E-timing	130	-	**116.5** (130:100)	116.0 ± 1.1
E_1	**0.13** (0:0.8)	0.21 ± 0.09	**0.22** (0:0.5)	0.23 ± 0.03
E_2	**0.0071** (0:0.1)	0.0064 ± 0.0029	**0.0056** (0:0.1)	0.0078 ± 0.0046
T_b (basal temp, ºC)	**860.5** (600:950)	760.7 ± 92.8	850	
Time Step	1		1	
Run time (Ma)	150		150	
Number of models	10224		9504	
Lowest misfit, μ	1334.2		1325.5	
Number of Data	28		28	
Misfit type	χ^2		χ^2	
Free parameters	5		5	
Models/Iterations	144/70		144/65	
Resample Rate	63%		70%	

Table 2: Pecube-NA inversion results for sensitivity test and full inversions. Values separated by a colon are the prior search ranges during the NA sampling stage while those in bold are the best-fit parameter values (lowest misfit). Mean and standard deviation represent the resampling results from the NA appraisal of the model ensemble. *R* = relief amplitude; τ = erosional timescale; E-timing is the time of exhumation rate change; E_1 and E_2 = exhumation rate 1 and exhumation rate 2. See text for details.

Model inversion 1-TSW (fig. 10) shows paleo-relief greater than ~60% of the modern (1.62 ± 0.08) is required to explain the AHe ages. The *τ* (erosional timescale) parameter is a primary control on the evolution of relief, as the relief amplitude and erosional timescale show a positive correlation. The large positive value for *τ* suggests exponentially rapid relief evolution following the main exhumation phase.

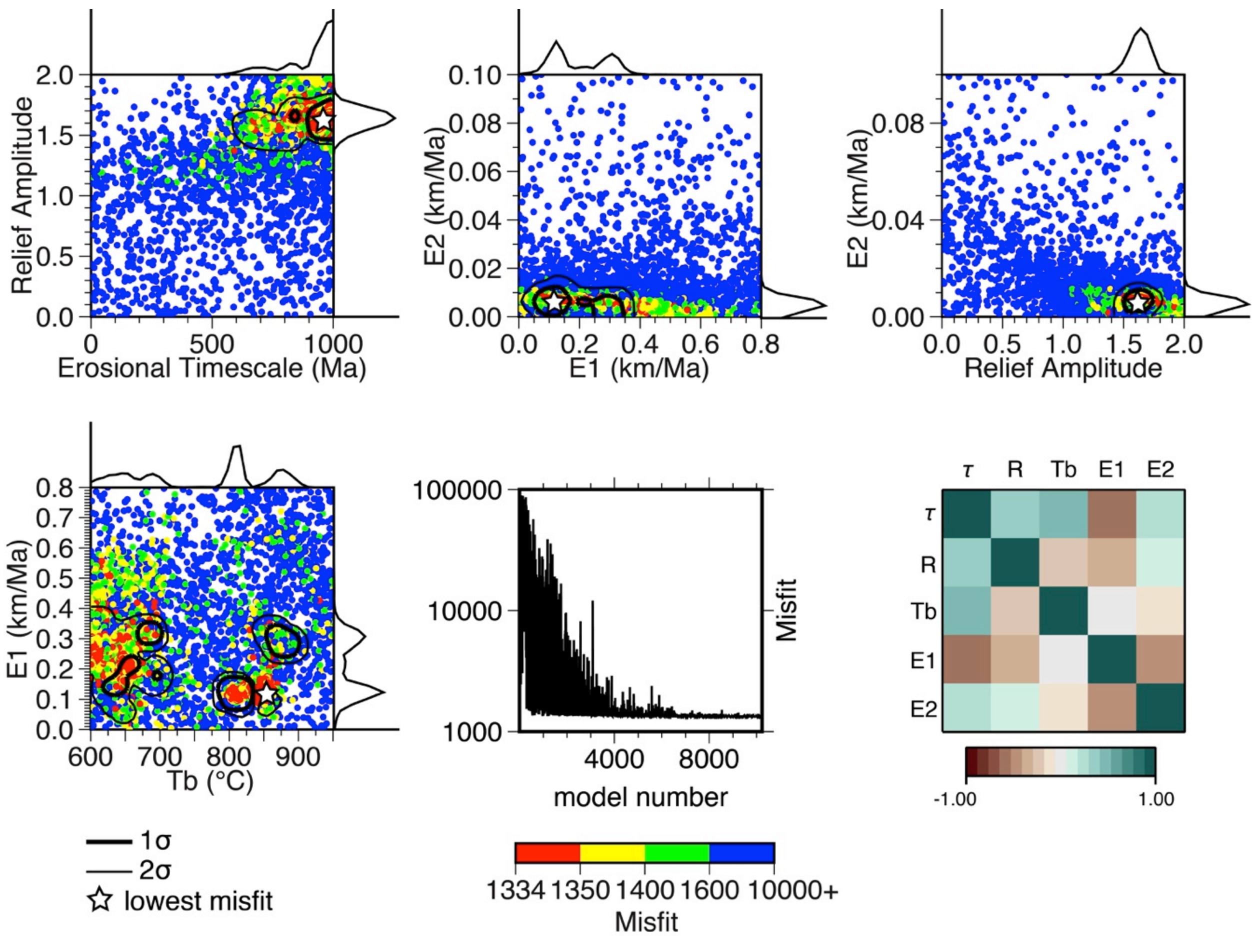

Figure 10: Pecube-NA inversion results for Run 1-TSW. Scatter plots are 2-D projections of the 5 dimensional parameter space on planes defined by combinations of two parameters. 1-D posterior curves show probability density within the parameter search range. See supplementary material for additional plots of other variables. Each dot represents a forward model from the inversion and is colored by the χ^2 misfit value. Stars denote the lowest misfit model while heavy/thin black lines are 1σ (67% confidence) and 2σ (95% confidence) errors, respectively. Bottom middle panel shows misfit evolution and convergence during the inversion and the bottom right shows the correlation matrix between difference parameters between -1 to +1 signifying strong (negative) anti-correlation or positive correlation, with values near zero having no relationship. Pecube physical modeling domain shown in fig. 13 inset box, see text for discussion.

Inversion 1-C results are in good agreement with inversion 1-TSW, where the only difference is in the delayed timing in exhumation rate change at ~116 Ma (lowest misfit), which appropriately constrains the predicted relief reduction to be slightly lower (fig. 11). A two-stage exhumation scenario was applied for simplicity and because more complicated exhumation histories are unnecessary to explain the data. If exhumation is shorter in duration, i.e. 150 to 130 Ma versus 150 to ~115 Ma, the required paleo-relief is also greater. Both inversions suggest exhumation was never extremely rapid during this time, on the order of ~100-200 m/My during the primary phase and very low since the Early Cretaceous at ≤10 m/My (table 2). The E_1-E_2 scatterplot (fig. 11; table 2) shows that the secondary phase of exhumation is required to be very low at ~6 ± 3 m/My, regardless of what the E_1 exhumation rate is. The geothermal gradient, which is controlled by the basal temperature of the crust (T_b) shows two distinct regions of either a cooler or hotter Moho temperature where neither has a clear relationship with the primary exhumation phase (E_1), however larger values of *R* require a lower (E_2) exhumation rate. The best-fit model has a basal temperature of 860°C, which is in agreement with local geochemical data [e.g. *Ionov et al.*, 1998; *Ancuta*, 2017] and produces a geothermal gradient in agreement with paleo- and modern estimates of 15 and 21 °C/km, respectively [*Ionov et al.*, 1998; *Kopylova et al.,* 1995; *Lysak and* Dorofeeva, 2003; West *et al.,* 2013].

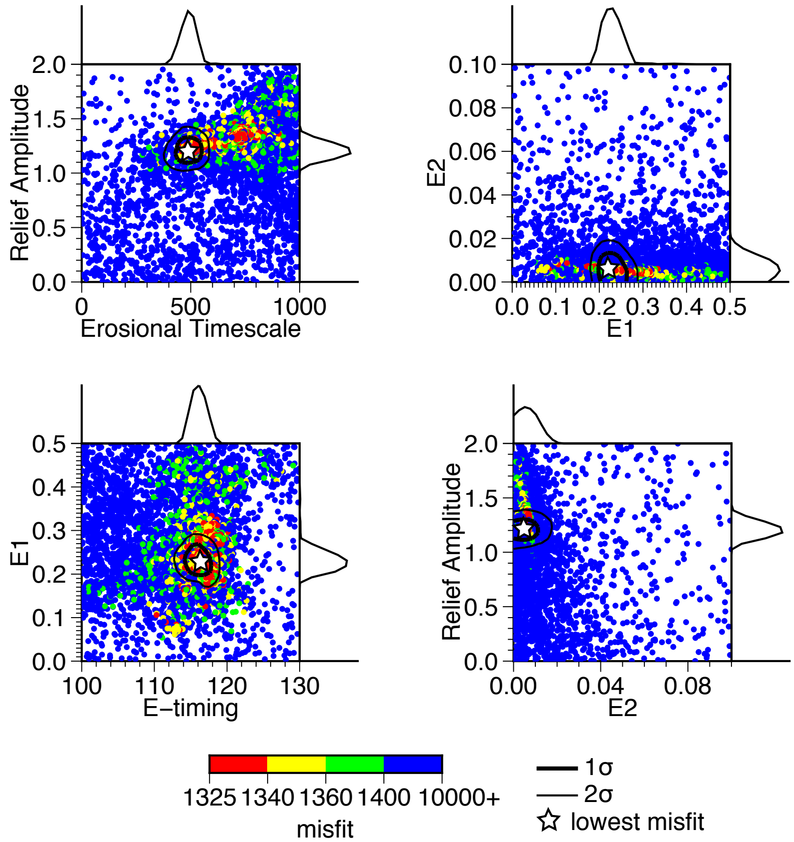

Figure 11: Pecube-NA Run 1-C inversion results for 9504 models. The same figure scheme as figure 9. The difference between Run 1-TSW is that the exhumation rate change timing is allowed free in this inversion.

The misfit values reported for the full inversions are higher than the sensitivity inversion because the sensitivity test allowed much greater variance in the synthetic age uncertainties. The full inversions used the analytical error, which is typically ≤ 2 Ma. The observed and predicted ages agree very well, generally within 2%, except for a few cases where the reported AHe age is slightly older (~10%) than the predicted age, which drove the misfit up (fig. 12; suppl. table S4). The reported multi-grain aliquot AHe data from *West et al.* [2013] were over-predicted and were the main contributors to the higher overall misfit values.

We ran Pecube forward models using the best-fit parameters of inversion 1-TSW to predict model regional AHe cooling ages. Figure 12 shows observed versus predicted cooling ages using the best-fit parameters from inversion 1-TSW for the western Hangay. The major discrepancy in age agreement (higher associated misfit) lies between the *West et al.* [2013] multi-grain aliquot AHe ages and those modeled at high elevations (fig. 12B). This is likely due to the cooling age 'averaging' bias from using multiple grain aliquots, and in combination with the known scatter in slowly cooled samples, produces ages that do not adequately represent the 'true' single grain cooling ages. In this case, it seems that the *West et al.* [2013] AHe ages are younger in comparison to nearby samples from this study. The elevation for the highest samples is also under-predicted (fig. 12D), which may be convolved with the errors associated with the age prediction itself, or indicates that the predicted relief evolution is too simplistic and does not fully capture the nuanced topography. The latter may very well be the case since the relict planation surfaces represent fragments of topography that were never eroded and are thus difficult to reproduce numerically. The same can be said for potential outlier ages from our dataset that are anomalously old and not readily explained by radiation damage, grain size, etc., which cannot be fit adequately.

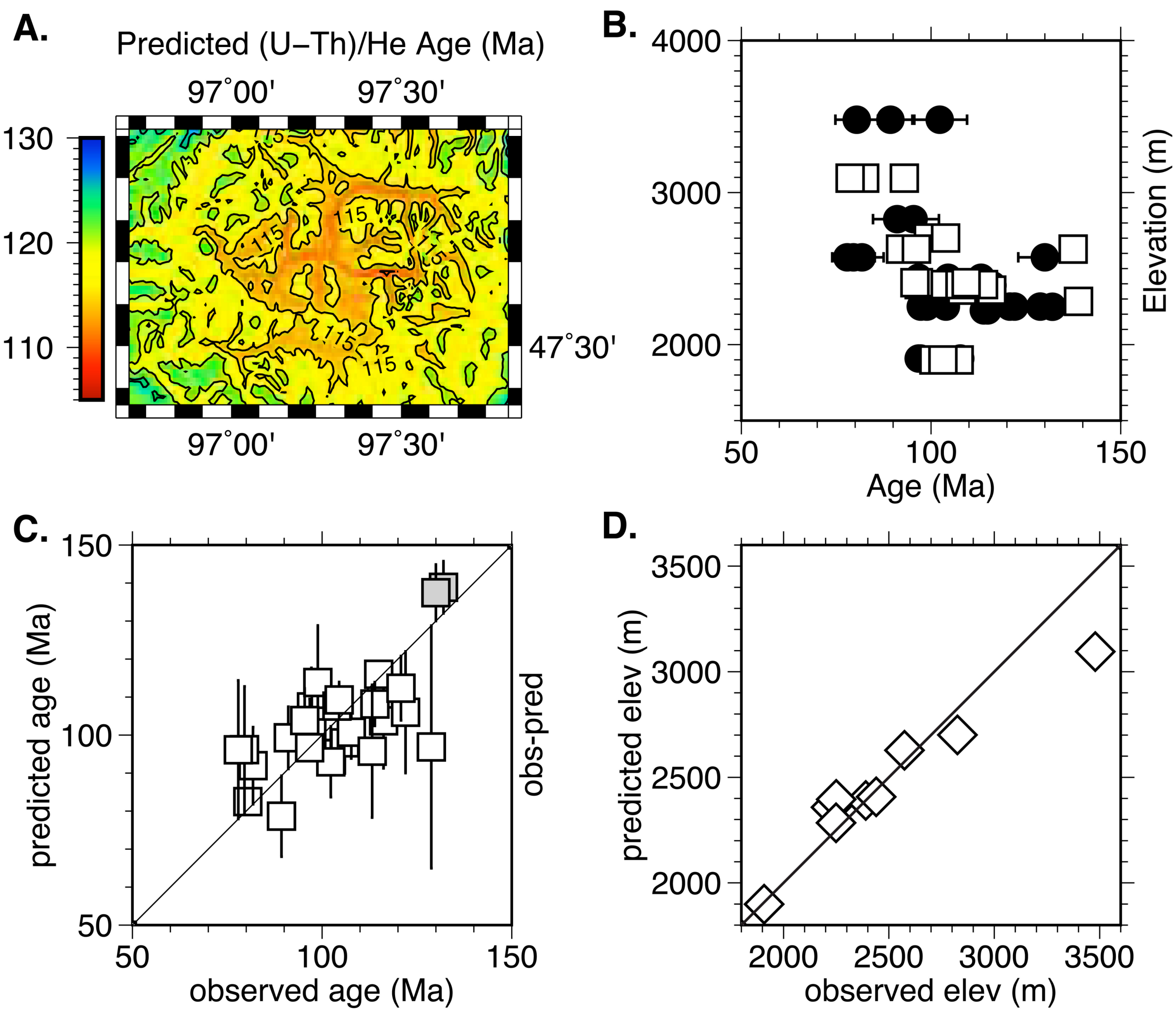

Figure 12: **(A)** Contoured age map (5 Ma interval) of Pecube-NA Run 1-TSW in the western Hangay (see fig. 13 for location, inset box). **(B)** Observed and predicted cooling ages and corresponding elevations are in good agreement except mainly at the highest elevations. Forward modeled using Pecube inversion modeled best-fit or maximum likelihood inversion values. Black circles are observed single-grain age replicates with errors, while squares are predicted cooling ages. **(C)** 1-to-1 line for predicted vs. observed cooling ages; gray squares are AFT samples. Vertical lines at age points correspond to the absolute difference between predicted ages that were better numerical fits to observed ages, and those that were not. **(D)** observed versus predicted elevations using best-fit 1-TSW inversion relief scenario in Pecube forward model.

The optimum inversion 1-TSW model parameters for the western Hangay were held fixed and extrapolated to the entire Hangay and forward modeled (fig. 13). Four different model scenarios explored changes in effective elastic thickness. This was done to test the response to erosional unloading, which is magnified or isostatically-enhanced when the elastic thickness is low (in local isostatic equilibrium), compared to a high elastic thickness of 20 km or more (strong lithosphere). Regional variations in lithospheric thickness and mechanical properties, as well as varying depths of seismicity and changes in regional faulting character, cause effective elastic thickness variability in Mongolia [*Bayasgalan et al.,* 2005]. The Pecube-predicted age surface maps were resampled at the 10 km length scale to smooth age gradients (fig. 13). Contouring the predicted age surfaces allowed comparisons of regional cooling age spatial patterns. The effective elastic thickness from *Bayasgalan et al.* [2005] is shown in the upper right panel (Te of 6.1 km), while the other panels show results using elastic thicknesses of 0 (local isostasy), 15, and 20 km. Local isostasy (Te = 0) produces uniform predicted ages across the Hangay, closely following the topography but with less age variation in the broad sense (fig. 13). Increasing Te (panels 15 and 20 km) yield concentric 'bulls-eye' patterns of increasing cooling ages away from the range center with less topographic correlation. For comparison, a model of steady-state topography employing the best-fit exhumation rates shows expected age uniformity across the entire region and ages that are consistently older than those under relief-loss conditions. However, a steady-state topography model would likely require a slightly different exhumation history than the prescribed best-fit history of the inversion. The overall misfits for each model are fairly similar and fit the data within analytical error (reduced chi-squared misfit 0.8-0.9), demonstrating that varying Te has little effect on the match between observed and predicted ages for low exhumation rates. However, at the orogeny-scale an elastic thickness of 20 km yields a marginally better misfit compared to the other models, which agrees with the findings of *Bayasgalan et al.* [2005] that the elastic strength of the lithosphere increases away from the central Hangay.

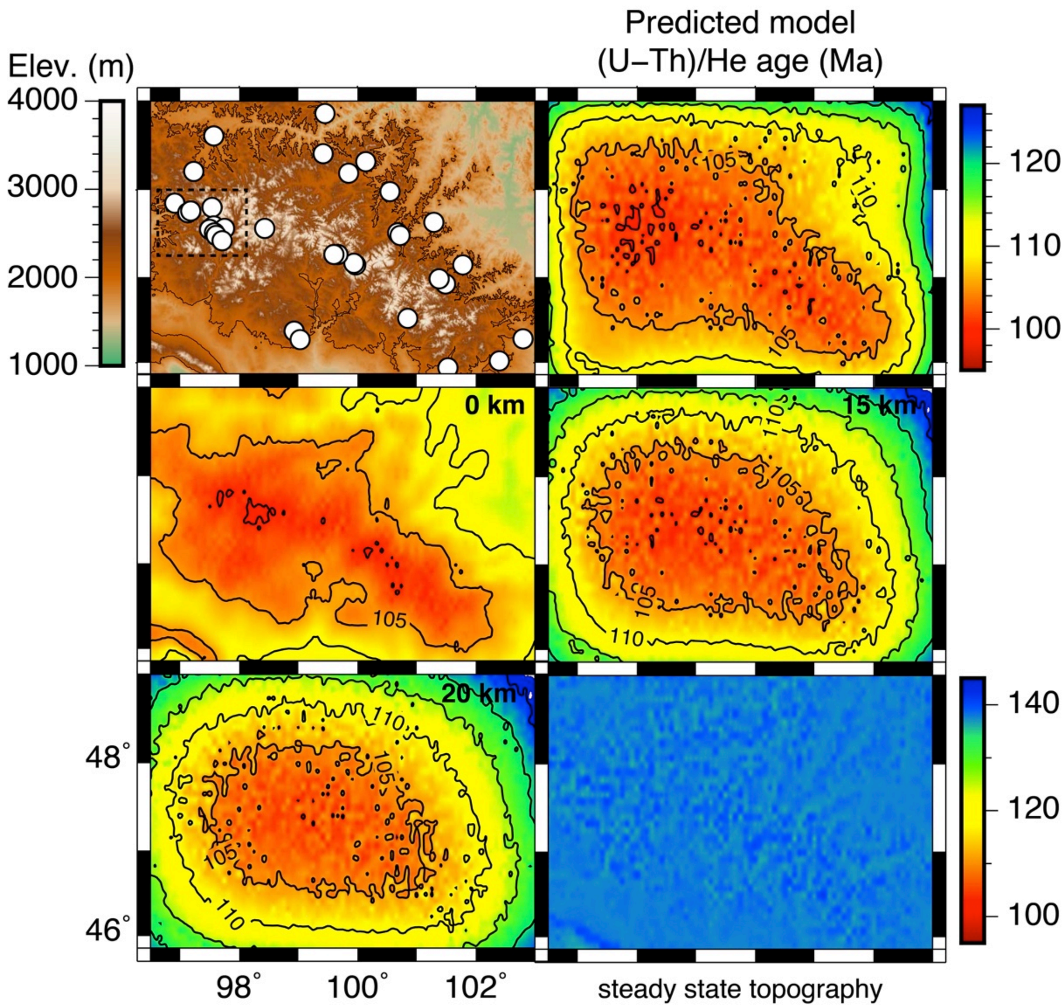

Figure 13: Pecube forward model age predictions using inversion run 1-TSW best-fit parameter values with the main exhumation stage from 150-130 Ma after *West et al.* [2013] model thermal history. Inset box shows location of western Hangay bounds used in Pecube-NA inversion. Regional forward models are resampled at 10 km to smooth ages and are shown with a 5 Ma contour interval. (Top left) Elevations from 90m SRTM DEM (2000 m elev. contoured) with white dots showing sample locations used in Pecube modeling of the entire Hangay, (top right) the ages predicted by the best-fit model results of inversion 1-TSW shown in table 1 (Te = 6.1 km). Other panels show the effects of varying the effective elastic thickness (Te) while holding all other best-fit variables constant. Note the age scale change for the steady-state topography model.

6. Discussion

Some first-order conclusions about the regional relief history of the Hangay can be made from the thermochronology and modeling results. Apatite (U-Th)/He cooling ages and regional patterns from this study indicate Mesozoic cooling based on spatial relationships across central

Mongolia. Relief lowering exposed younger ages at high peaks while valley bottoms are older, producing an orogen-scale, inverted age-elevation relationship but maintained valley-scale positive AERs. The steep trend of positive AERs also suggests a low elastic-plate thickness (<20 km), which has been previously advocated for the Hangay [*Bayasgalan et al.,* 2005]. These AER trends have been documented in other old, post-orogenic mountains in central Asia with similar exhumation histories, such as the Dabie Shan [*Reiners et al.,* 2003]. This age relationship is observed in the Hangay as well, where cooling ages are generally uniform in the mountain core, while away from the higher topography ages are slightly older.

The regional bedrock cooling age trends and the detrital AHe data point to relief reduction following the last major tectonic event in the Late Jurassic-Early Cretaceous. Cooling-age patterns are explained by preferential exposure of younger rocks at higher elevations through summit relief lowering from isostatically-enhanced erosion of the Hangay Mountains during the initial post-orogenic phase in the Cretaceous. One could argue that instead of relief lowering, recent surface uplift accompanied by some amount of erosion could produce similar age patterns. There is no evidence to support a Cenozoic history involving accelerated, high-magnitude (>1-2 km) erosion of the Hangay. Moderately higher erosion rates from basalt age data are only found in isolated cirques and glacial valleys (river headwaters regions), or valleys that have experienced local base-level changes due to Cenozoic basalt emplacement.

The suturing of Mongolia and collision with the Siberian craton created high mountains in central Mongolia in the early Mesozoic, which were then eroded rapidly in the Cretaceous, remaining as an erosional remnant landscape throughout the Cenozoic. Erosional proxies in the form of detrital cooling ages agree to first-order with thermo-kinematic models and indicate extended, low erosion since the end Mesozoic and that Jurassic-Early Cretaceous paleo-relief was greater than the present. Holding the current landscape geometry fixed through time, the current approximated mountain relief of the Hangay is approximately 2500 m, which would be approaching 4000 m in the Mesozoic using the modeled paleo-relief relative to current elevations. Relief 50-60% greater than the modern value would produce ancient elevations in the Hangay approaching 6000 m at the highest peaks, roughly on par with the modern Tian Shan to the southwest.

Exhumation rates estimated from Pecube inversions suggest a period of moderate exhumation in the Early Cretaceous followed by low rates of ~10 m/My since that time. This history agrees with shorter-term cosmogenic estimates of erosion and implies that the Hangay have been subject to a long regime of very slow erosion, similar to other old orogenic landscapes, such as the Appalachians in the eastern USA [e.g. *McKeon et al.,* 2014]. The high-elevation regions of the Hangay have experienced topographic rejuvenation because of recent enhanced erosion from alpine glaciation that is minimal in magnitude and regional extent (supplement fig. S2).

7. Conclusions

The termination of the Mongol-Okhotsk orogeny in the Cretaceous and synchronous rapid relief reduction produced the observed pattern of progressively older cooling ages away from the highest topography of the Hangay Mountains. Bedrock apatite (U-Th)/He age spatial patterns in the Hangay Mountains are reinforced by detrital (U-Th)/He ages and indicate <2 km of exhumation since the Cretaceous, while detrital age distributions and geomorphic relationships suggest that current elevations between ~1600-1800 m at the Hangay margins are the current focus of incision across the landscape. Pecube thermo-kinematic inversions and detrital age modeling suggests topographic relief was up to 60% greater than the modern relief during the late Mesozoic. The magnitude of relief loss in Pecube model inversions is highly correlated with the timing of the shift to very low exhumation rates, with more extended high-rate periods (i.e. delayed exhumation rate change) requiring less relief loss. Relief has presumably been stable throughout the Cenozoic due to high aridity, with a modest amount of surface uplift probably occurring in the Oligocene-Miocene. The Hangay Mountain landscape is an old feature that has recently undergone surface uplift of a few hundred meters, which locally imprinted a younger, more dramatic landscape through glacial cirque cutting in the highest topography. This mountain belt is an excellent example of a relict erosional landscape and demonstrates that mature topography can endure for prolonged periods when there is little forcing from tectonics, climate, or surface processes.

Acknowledgements

The authors thank two anonymous reviewers for thorough comments and suggestions to improve the manuscript. We thank M. Jolivet for comments on an earlier version of this manuscript. We also thank D. Whipp and F. Herman for discussions and for supplying various bits of code and J. Braun and M. Sambridge for conversations about Pecube and the Neighborhood Algorithm. We would also like to thank A. Pacheco of Lehigh University HPC for support with the Lehigh Corona computing cluster. Final inversions were run through XSEDE and the SDSC Gordon/Comet clusters and the UT-Austin TACC Stampede cluster. This study was supported by a grant from the National Science Foundation CD program grant EAR-1009702. The data used are listed in the references, figures, tables, and supplements provided.

References

Ancuta, L. D. (2017), Toward an Improved Understanding of Intraplate Uplift and Volcanism: Geochronology and Geochemistry of Intraplate Volcanic Rocks and Lower-Crustal Xenoliths, 207 pp, Lehigh University, Bethlehem, PA.

Baldwin, J. A., K. X. Whipple, and G. E. Tucker (2003), Implications of the shear stress river incision model for the timescale of postorogenic decay of topography, *Journal of Geophysical Research: Solid Earth (1978–2012)*, *108*(B3).

Bayasgalan, A., J. Jackson, and D. McKenzie (2005), Lithosphere rheology and active tectonics in Mongolia: relations between earthquake source parameters, gravity and GPS measurements, *Geophysical Journal International*, *163*(3), 1151-1179.

Beucher, R., P. Beek, J. Braun, and G. E. Batt (2012), Exhumation and relief development in the Pelvoux and Dora‐Maira massifs (western Alps) assessed by spectral analysis and inversion of thermochronological age transects, *Journal of Geophysical Research: Earth Surface*, *117*(F3).

Braun, J. (2002), Quantifying the effect of recent relief changes on age-elevation relationships, *Earth and Planetary Science Letters*, *200*(3-4), 331-343.

Braun, J. (2003), Pecube: a new finite-element code to solve the 3D heat transport equation including the effects of a time-varying, finite amplitude surface topography, *Computers & Geosciences*, *29*(6), 787-794.

Braun, J., and X. Robert (2005), Constraints on the rate of post-orogenic erosional decay from low-temperature thermochronological data: application to the Dabie Shan, China, *Earth Surface Processes and Landforms*, *30*(9), 1203-1225.

Braun, J., P. van der Beek, P. Valla, X. Robert, F. Herman, C. Glotzbach, V. Pedersen, C. Perry, T. Simon-Labric, and C. Prigent (2012), Quantifying rates of landscape evolution and tectonic processes by thermochronology and numerical modeling of crustal heat transport using PECUBE, *Tectonophysics*, *524-525*, 1-28.

Brewer, I., D. Burbank, and K. Hodges (2003), Modelling detrital cooling‐age populations: Insights from two Himalayan catchments, *Basin Research*, *15*(3), 305-320.

Brocklehurst, S. H., and K. X. Whipple (2004), Hypsometry of glaciated landscapes, *Earth Surface Processes and Landforms*, *29*(7), 907-926.

Cai, K., M. Sun, B.-m. Jahn, W. Xiao, C. Yuan, X. Long, H. Chen, and D. Tumurkhuu (2015), A synthesis of zircon U–Pb ages and Hf isotopic compositions of granitoids from Southwest Mongolia: Implications for crustal nature and tectonic evolution of the Altai Superterrane, *Lithos*, *232*, 131-142.

Carlson, R. W., and D. Ionov (2014), Lithospheric Mantle Contribution to High Topography in Central Mongolia, American Geophysical Union, Fall Meeting 2014, abstract #T21A-4556, San Francisco, CA.

Caves, J. K., D. J. Sjostrom, H. T. Mix, M. J. Winnick, and C. P. Chamberlain (2014), Aridification of Central Asia and uplift of the Altai and Hangay Mountains, Mongolia: Stable isotope evidence, *American Journal of Science*, *314*(8), 1171-1201.

Chen, M., F. Niu, Q. Liu, and J. Tromp (2015), Mantle-driven uplift of Hangai Dome: New seismic constraints from adjoint tomography, *Geophysical Research Letters*, *42*(17), 6967-6974.

Cogné, J.-P., V. A. Kravchinsky, N. Halim, and F. Hankard (2005), Late Jurassic-Early Cretaceous closure of the Mongol-Okhotsk Ocean demonstrated by new Mesozoic palaeomagnetic results from the Trans-Baikal area (SE Siberia), *Geophysical Journal International*, *163*(2), 813-832.

Cunningham, W. D. (2001), Cenozoic normal faulting and regional doming in the southern Hangay region, Central Mongolia: implications for the origin of the Baikal rift province, *Tectonophysics*, *331*(4), 389-411.

De Grave, J., M. M. Buslov, P. Van Den Haute, J. Metcalf, B. Dehandschutter, and M. O. McWilliams (2009), Multi-method chronometry of the Teletskoye graben and its basement, Siberian Altai Mountains: new insights on its thermo-tectonic evolution, *Geological Society, London, Special Publications*, *324*(1), 237-259.

Devyatkin, E. V. (1975), Neotectonic structures of western Mongolia (in Russian): Mesozoic and Cenozoic Tectonics and Magmatism of Mongolia: Moscow, Nauka, 264-282.

Egholm, D. L., M. F. Knudsen, and M. Sandiford (2013), Lifespan of mountain ranges scaled by feedbacks between landsliding and erosion by rivers, *Nature*, *498*(7455), 475-478.

Ehlers, T. A., A. Szameitat, E. Enkelmann, B. J. Yanites, and G. J. Woodsworth (2015), Identifying spatial variations in glacial catchment erosion with detrital thermochronology, *Journal of Geophysical Research: Earth Surface*, *120*(6), 1023-1039.

Farley, K. A. (2000), Helium diffusion from apatite; general behavior as illustrated by Durango fluorapatite, *Journal of Geophysical Research*, *105*(B2), 2903-2914.

Farley, K. A., D. L. Shuster, and R. A. Ketcham (2011), U and Th zonation in apatite observed by laser ablation ICPMS, and implications for the (U–Th)/He system, *Geochimica et Cosmochimica Acta*, *75*(16), 4515-4530.

Fischer, K. M. (2002), Waning buoyancy in the crustal roots of old mountains, *Nature*, *417*(6892), 933-936.

Fitzgerald, P. G., S. L. Baldwin, L. E. Webb, and P. B. O'Sullivan (2006), Interpretation of (U–Th)/He single grain ages from slowly cooled crustal terranes: A case study from the Transantarctic Mountains of southern Victoria Land, *Chemical Geology*, *225*(1-2), 91-120.

Flowers, R. M., R. A. Ketcham, D. L. Shuster, and K. A. Farley (2009), Apatite (U–Th)/He thermochronometry using a radiation damage accumulation and annealing model, *Geochimica et Cosmochimica Acta*, *73*(8), 2347-2365.

Gautheron, C., L. Tassan-Got, J. Barbarand, and M. Pagel (2009), Effect of alpha-damage annealing on apatite (U–Th)/He thermochronology, *Chemical Geology*, *266*(3), 157-170.

Gillespie, J., S. Glorie, W. Xiao, Z. Zhang, A. S. Collins, N. Evans, B. McInnes, and J. De Grave (2015), Mesozoic reactivation of the Beishan, southern Central Asian Orogenic Belt: Insights from low-temperature thermochronology, *Gondwana Research*, *43*(March 2017), 107-122.

Glorie, S., and J. De Grave (2016), Exhuming the Meso–Cenozoic Kyrgyz Tianshan and Siberian Altai-Sayan: A review based on low-temperature thermochronology, *Geoscience Frontiers*, *7*(2), 155-170.

Glotzbach, C., P. A. Van Der Beek, and C. Spiegel (2011), Episodic exhumation and relief growth in the Mont Blanc massif, Western Alps from numerical modelling of thermochronology data, *Earth and Planetary Science Letters*, *304*(3), 417-430.

Hendrix, M. S., S. A. Graham, A. R. Carroll, E. R. Sobel, C. L. McKnight, B. J. Schulein, and Z. Wang (1992), Sedimentary record and climatic implications of recurrent deformation in the Tian Shan: Evidence from Mesozoic strata of the north Tarim, south Junggar, and Turpan basins, northwest China, *Geological Society of America Bulletin*, *104*(1), 53-79.

Herman, F., E. J. Rhodes, J. Braun, and L. Heiniger (2010), Uniform erosion rates and relief amplitude during glacial cycles in the Southern Alps of New Zealand, as revealed from OSL-thermochronology, *Earth and Planetary Science Letters*, *297*(1), 183-189.

Hetzel, R., I. Dunkl, V. Haider, M. Strobl, H. von Eynatten, L. Ding, and D. Frei (2011), Peneplain formation in southern Tibet predates the India-Asia collision and plateau uplift, *Geology*, *39*(10), 983-986.

Hopkins, C. E. (2012), Beryllium-10 derived erosion rates from the Hangay Mountains, Mongolia: landscape evolution in a periglacially-dominated continental interior, 48 pp, Georgia Institute of Technology.

Hunt, A. C., I. J. Parkinson, N. B. W. Harris, T. L. Barry, N. W. Rogers, and M. Yondon (2012), Cenozoic Volcanism on the Hangai Dome, Central Mongolia: Geochemical Evidence for Changing Melt Sources and Implications for Mechanisms of Melting, *Journal of Petrology*.

Idleman, B. D., P. K. Zeitler, and K. T. McDannell (2018), Characterization of helium release from apatite by continuous ramped heating, *Chemical Geology*, *476*, 223-232. https://doi.org/10.1016/j.chemgeo.2017.11.019

Ionov, D. A., S. Y. O'Reilly, and W. L. Griffin (1998), A geotherm and lithospheric section for central Mongolia (Tariat region), *Mantle dynamics and plate interactions in East Asia*, 127-153.

Jahn, B., F. Wu, and B. Chen (2000), Granitoids of the Central Asian Orogenic Belt and continental growth in the Phanerozoic, *Geological Society of America Special Papers*, *350*, 181-193.

Jasra, A., D. Stephens, K. Gallagher, and C. Holmes (2006), Analysis of geochronological data with measurement error using Bayesian mixtures, *Mathematical Geology*, *38*(3), 269-300.

Johnson, C., K. Constenius, S. Graham, G. Mackey, T. Menotti, A. Payton, and J. Tully (2015), Subsurface evidence for late Mesozoic extension in western Mongolia: tectonic and petroleum systems implications, *Basin Research*, *27*(3), 272-294.

Jolivet, M. (2017), Mesozoic tectonic and topographic evolution of Central Asia and Tibet: a preliminary synthesis, *Geological Society, London, Special Publications*, *427*(1), 19-55.

Jolivet, M., S. Arzhannikov, A. Arzhannikova, A. Chauvet, R. Vassallo, and R. Braucher (2013), Geomorphic Mesozoic and Cenozoic evolution in the Oka-Jombolok region (East Sayan ranges, Siberia), *Journal of Asian Earth Sciences*, *62*, 117-133.

Jolivet, M., S. Bourquin, G. Heilbronn, C. Robin, L. Barrier, M.-P. Dabard, Y. Jia, E. De Pelsmaeker, and B. Fu (2015), The Upper Jurassic–Lower Cretaceous alluvial-fan deposits of the Kalaza Formation (Central Asia): tectonic pulse or increased aridity?, *Geological Society, London, Special Publications*, *427*, SP427. 426.

Jolivet, M., J.-F. Ritz, R. Vassallo, C. Larroque, R. Braucher, M. Todbileg, A. Chauvet, C. Sue, N. Arnaud, and R. De Vicente (2007), Mongolian summits: an uplifted, flat, old but still preserved erosion surface, *Geology*, *35*(10), 871-874.

Jolivet, M., T. De Boisgrollier, C. Petit, M. Fournier, V. Sankov, J. C. Ringenbach, L. Byzov, A. Miroshnichenko, S. N. Kovalenko, and S. Anisimova (2009), How old is the Baikal Rift Zone? Insight from apatite fission track thermochronology, *Tectonics*, *28*(3).

Koppes, M. N., and D. R. Montgomery (2009), The relative efficacy of fluvial and glacial erosion over modern to orogenic timescales, *Nature Geoscience*, *2*(9), 644-647.

Kopylova, M. G., S. Y. O'Reilly, and Y. S. Genshaft (1995), Thermal state of the lithosphere beneath Central Mongolia: evidence from deep-seated xenoliths from the Shavaryn-Saram volcanic centre in the Tariat depression, Hangai, Mongolia, *Lithos*, *36*(3,Äì4), 243-255.

Kröner, A., E. Hegner, B. Lehmann, J. Heinhorst, M. T. D. Wingate, D. Y. Liu, and P. Ermelov (2008), Palaeozoic arc magmatism in the Central Asian Orogenic Belt of Kazakhstan: SHRIMP zircon ages and whole-rock Nd isotopic systematics, *Journal of Asian Earth Sciences*, *32*(2-4), 118-130.

Landman, R. L. (2007), Petrologic constraints on the sources of granites from the Hangay Mountains, central Mongolia, 73 pp, Amherst College.

Lehmann, J., K. Schulmann, O. Lexa, M. Corsini, A. Kroner, P. Stipska, D. Tomurhuu, and D. Otgonbator (2010), Structural constraints on the evolution of the Central Asian Orogenic Belt in SW Mongolia, *American Journal of Science*, *310*(7), 575-628.

Lehmkuhl, F. (1998), Quaternary glaciations in central and western Mongolia, *Journal of Quaternary Science*, *13*(6), 153-167.

Lehmkuhl, F., M. Klinge, and G. Stauch (2004), The extent of Late Pleistocene glaciations in the Altai and Khangai Mountains, in *Developments in Quaternary Sciences*, edited by J. Ehlers and P. L. Gibbard, pp. 243-254, Elsevier.

Lehmkuhl, F., and A. Lang (2001), Geomorphological investigations and luminescence dating in the southern part of the Khangay and the Valley of the Gobi Lakes (Central Mongolia), *Journal of Quaternary Science*, *16*(1), 69-87.

Logachev, N. A., E. V. Devyatkin, E. M. Malaeva, and e. al. (1982), Cenozoic Deposits in the Taryat Basin and in the Chulutu R. Valley, Central Khangai, *Izv. AN SSSR. Ser. Geol.*, *no. 8*, 76-86.

Lysak, S., and R. Dorofeeva (2003), Thermal state of lithosphere in Mongolia, *Russ. Geol. Geophys*, *44*(9), 893-903.

Mancktelow, N. S., and B. Grasemann (1997), Time-dependent effects of heat advection and topography on cooling histories during erosion, *Tectonophysics*, *270*(3), 167-195.

Matmon, A., P. R. Bierman, J. Larsen, S. Southworth, M. Pavich, and M. Caffee (2003), Temporally and spatially uniform rates of erosion in the southern Appalachian Great Smoky Mountains, *Geology*, *31*(2), 155-158.

McDannell, K. T. (2017), Methods and application of deep-time thermochronology: Insights from slowly cooled terranes of Mongolia and the North American craton. Theses and Dissertations. 2721. 261 p., Lehigh University, Bethlehem, Pennsylvania. https://preserve.lehigh.edu/etd/2721

McDannell, K. T., P. K. Zeitler, D. G. Janes, B. D. Idleman, and A. K. Fayon (2018), Screening apatites for (U-Th)/He thermochronometry via continuous ramped heating: He age components and implications for age dispersion, *Geochimica et Cosmochimica Acta*, *223*, 90-106. https://doi.org/10.1016/j.gca.2017.11.031

McDowell, F. W., W. C. McIntosh, and K. A. Farley (2005), A precise 40 Ar–39 Ar reference age for the Durango apatite (U–Th)/He and fission-track dating standard, *Chemical Geology*, *214*(3), 249-263.

McKeon, R. E., P. K. Zeitler, F. J. Pazzaglia, B. D. Idleman, and E. Enkelmann (2014), Decay of an old orogen: Inferences about Appalachian landscape evolution from low-temperature thermochronology, *Geological Society of America Bulletin*, *126*(1-2), 31-46.

Meltzer, A., et al. (2012), Intracontinental Deformation and Surface Uplift-Geodynamic Evolution of the Hangay Dome, Mongolia Central Asia, American Geophysical Union, Fall Meeting 2012, abstract #T12A-05, San Francisco, CA.

Meltzer, A., et al. (2015), Betwixt and Between: Structure and Evolution of Central Mongolia, American Geophysical Union, Fall Meeting 2015, abstract #T22A-05, San Francisco, CA.

Molnar, P., and P. Tapponnier (1975), Cenozoic tectonics of Asia: effects of a continental collision, *Science*, *189*(4201), 419-426.

Molnar, P., and P. England (1990), Late Cenozoic uplift of mountain ranges and global climate change: chicken or egg?, *Nature*, *346*(6279), 29-34.

Molnar, P., W. R. Boos, and D. S. Battisti (2010), Orographic controls on climate and paleoclimate of Asia: thermal and mechanical roles for the Tibetan Plateau, *Annual Review of Earth and Planetary Sciences*, *38*(1), 77.

Montgomery, D. R., and M. T. Brandon (2002), Topographic controls on erosion rates in tectonically active mountain ranges, *Earth and Planetary Science Letters*, *201*(3), 481-489.

Petit, C., C. Tiberi, A. Deschamps, and J. Déverchere (2008), Teleseismic traveltimes, topography and the lithospheric structure across central Mongolia, *Geophysical Research Letters*, *35*(11).

Petit, C., J. Deverchere, E. Calais, V. San'kov, and D. Fairhead (2002), Deep structure and mechanical behavior of the lithosphere in the Hangai-Hovsgol region, Mongolia: new constraints from gravity modeling, *Earth and Planetary Science Letters*, *197*(3), 133-149.

Raymo, M. E., and W. F. Ruddiman (1992), Tectonic forcing of late Cenozoic climate. *Nature*, 359(6391), 117-122.

Reiners, P. W., and S. Nicolescu (2006), Measurement of parent nuclides for (U-Th)/He chronometry by solution sector ICP-MS *ARHDL Report 3.0*, University of Arizona.

Reiners, P. W., Z. Zhou, T. A. Ehlers, C. Xu, M. T. Brandon, R. A. Donelick, and S. Nicolescu (2003), Post-orogenic evolution of the Dabie Shan, eastern China, from (U-Th)/He and fission-track thermochronology, *American Journal of Science*, *303*(6), 489-518.

Reverman, R. L., M. G. Fellin, F. Herman, S. D. Willett, and C. Fitoussi (2012), Climatically versus tectonically forced erosion in the Alps: Thermochronometric constraints from the Adamello Complex, Southern Alps, Italy, *Earth and Planetary Science Letters*, *339*, 127-138.

Rickwood, P., and M. Sambridge (2006), Efficient parallel inversion using the Neighbourhood Algorithm, *Geochemistry, Geophysics, Geosystems*, *7*(11).

Ruhl, K. W., and K. V. Hodges (2005), The use of detrital mineral cooling ages to evaluate steady state assumptions in active orogens: An example from the central Nepalese Himalaya, *Tectonics*, *24*(4), TC4015.

Sahagian, D., A. Proussevitch, L. D. Ancuta, B. D. Idleman, and P. K. Zeitler (2016), Uplift of Central Mongolia Recorded in Vesicular Basalts, *The Journal of Geology*, *124*(4), 435-445.

Sambridge, M. (1999a), Geophysical inversion with a neighbourhood algorithm—I. Searching a parameter space, *Geophysical Journal International*, *138*(2), 479-494.

Sambridge, M. (1999b), Geophysical inversion with a neighbourhood algorithm—II. Appraising the ensemble, *Geophysical Journal International*, *138*(3), 727-746.

Shuster, D. L., R. M. Flowers, and K. A. Farley (2006), The influence of natural radiation damage on helium diffusion kinetics in apatite, *Earth and Planetary Science Letters*, *249*(3-4), 148-161.

Smith, S. G., K. W. Wegmann, L. D. Ancuta, J. C. Gosse, and C. E. Hopkins (2016), Paleotopography and erosion rates in the central Hangay Dome, Mongolia: Landscape evolution since the mid-Miocene, *Journal of Asian Earth Sciences*, *125*, 37-57.

Stachnik, J. C., A. Meltzer, S. Souza, U. Munkhuu, B. Tsaagan, and R. M. Russo (2014), Lithospheric Structure Beneath the Hangay Dome, Central Mongolia, in *American Geophysical Union*, AGU abstract T21A-4555, San Francisco.

Stock, G. M., T. A. Ehlers, and K. A. Farley (2006), Where does sediment come from? Quantifying catchment erosion with detrital apatite (U-Th)/He thermochronometry, *Geology*, *34*(9), 725-728.

Stock, J. D., and D. R. Montgomery (1996), Estimating palaeorelief from detrital mineral age ranges, *Basin Research*, *8*(3), 317-327.

Stosch, H. G., D. A. Ionov, I. S. Puchtel, S. J. G. Galer, and A. Sharpouri (1995), Lower crustal xenoliths from Mongolia and their bearing on the nature of the deep crust beneath central Asia, *Lithos*, *36*(3–4), 227-242.

Strahler, A. N. (1952), Hypsometric (area-altitude) analysis of erosional topography, *Geological Society of America Bulletin*, *63*(11), 1117-1142.

Stüwe, K., L. White, and R. Brown (1994), The influence of eroding topography on steady-state isotherms. Application to fission track analysis, *Earth and Planetary Science Letters*, *124*(1-4), 63-74.

Tiberi, C., A. Deschamps, J. Déverchère, C. Petit, J. Perrot, D. Appriou, V. Mordvinova, T. Dugaarma, M. Ulzibaat, and A. Artemiev (2008), Asthenospheric imprints on the lithosphere in Central Mongolia and Southern Siberia from a joint inversion of gravity and seismology (MOBAL experiment), *Geophysical Journal International*, *175*(3), 1283-1297.

Tomurtogoo, O., ed., 1999, Geological Map of Mongolia. Mongolian Academy of Sciences, 1:1,000,000.

Tomurtogoo, O., B. Windley, A. Kröner, G. Badarch, and D. Liu (2005), Zircon age and occurrence of the Adaatsag ophiolite and Muron shear zone, central Mongolia: constraints on the evolution of the Mongol–Okhotsk ocean, suture and orogen, *Journal of the Geological Society*, *162*(1), 125-134.

Valla, P. G., F. Herman, P. A. van der Beek, and J. Braun (2010), Inversion of thermochronological age-elevation profiles to extract independent estimates of denudation and relief history — I: Theory and conceptual model, *Earth and Planetary Science Letters*, *295*(3-4), 511-522.

van der Beek, P., D. Delvaux, P. Andriessen, and K. Levi (1996), Early Cretaceous denudation related to convergent tectonics in the Baikal region, SE Siberia, *Journal of the Geological Society*, *153*(4), 515-523.

van der Beek, P. A., P. G. Valla, F. Herman, J. Braun, C. Persano, K. J. Dobson, and E. Labrin (2010), Inversion of thermochronological age–elevation profiles to extract independent estimates of denudation and relief history — II: Application to the French Western Alps, *Earth and Planetary Science Letters*, *296*(1–2), 9-22.

Van der Voo, R., D. J. J. van Hinsbergen, M. Domeier, W. Spakman, and T. H. Torsvik (2015), Latest Jurassic–earliest Cretaceous closure of the Mongol-Okhotsk Ocean: A paleomagnetic and seismological-tomographic analysis, *Geological Society of America Special Papers*, *513*.

Vassallo, R., M. Jolivet, J. F. Ritz, R. Braucher, C. Larroque, C. Sue, M. Todbileg, and D. Javkhlanbold (2007), Uplift age and rates of the Gurvan Bogd system (Gobi-Altay) by apatite fission track analysis, *Earth and Planetary Science Letters*, *259*(3,Äì4), 333-346.

Vermeesch, P. (2010), HelioPlot, and the treatment of overdispersed (U–Th–Sm)/He data, *Chemical Geology*, *271*(3–4), 108-111.

Vermeesch, P. (2012), On the visualisation of detrital age distributions, *Chemical Geology*, *312*, 190-194.

Wegmann, K. W., et al. (2014), Geomorphic and Fish Genetics Constraints on Late Cenozoic Long Wavelength Topographic Evolution of the Hangay Mountains, Central Mongolia, American Geophysical Union, Fall Meeting 2014, abstract #T21A-4560, San Francisco, CA.

West, A. J., M. Fox, R. T. Walker, A. Carter, T. Harris, A. B. Watts, and B. Gantulga (2013), Links between climate, erosion, uplift, and topography during intracontinental mountain building of the Hangay Dome, Mongolia, *Geochemistry, Geophysics, Geosystems*, *14*(12), 5171-5193.

Whipp, D., T. Ehlers, J. Braun, and C. Spath (2009), Effects of exhumation kinematics and topographic evolution on detrital thermochronometer data, *Journal of Geophysical Research: Earth Surface*, *114*(F4).

Windley, B. F., and M. B. Allen (1993), Mongolian plateau: Evidence for a late Cenozoic mantle plume under central Asia, *Geology*, *21*(4), 295-298.

Windley, B. F., D. Alexeiev, W. Xiao, A. Kröner, and G. Badarch (2007), Tectonic models for accretion of the Central Asian Orogenic Belt, *Journal of the Geological Society*, *164*(1), 31-47.

Yang, Y.-T., Z.-X. Guo, C.-C. Song, X.-B. Li, and S. He (2015), A short-lived but significant Mongol–Okhotsk collisional orogeny in latest Jurassic–earliest Cretaceous, *Gondwana Research*, *28*(3), 1096-1116.

Yanovskaya, T., and V. Kozhevnikov (2003), 3D S-wave velocity pattern in the upper mantle beneath the continent of Asia from Rayleigh wave data, *Physics of the Earth and Planetary Interiors*, *138*(3), 263-278.

Yanshin, A. L. (1975), Mesozoic and Cenozoic tectonics and the magmatism of Mongolia: Joint Soviet-Mongolian scientific research geological expedition, *Transactions*, *11*, 308.

Yarmolyuk, V., B. Litvinovsky, V. Kovalenko, B.-M. Jahn, A. Zanvilevich, A. Vorontsov, D. Zhuravlev, V. Posokhov, D. Kuzmin, and G. Sandimirova (2001), Formation stages and sources of the peralkaline granitoid magmatism of the Northern Mongolia-Transbaikalia Rift Belt during the Permian and Triassic, *Petrology*, *9*(4), 302-328.

Yarmolyuk, V., et al. (2008), The age of the Khangai batholith and the problem of batholith formation in Central Asia, *Doklady Earth Sciences*, *423*(1), 1223-1228.

Yin, A. (2010), Cenozoic tectonic evolution of Asia: A preliminary synthesis, *Tectonophysics*, *488*(1), 293-325.

Zeitler, P. K., A. S. Meltzer, P. O. Koons, D. Craw, B. Hallet, C. P. Chamberlain, W. S. Kidd, S. K. Park, L. Seeber, and M. Bishop (2001), Erosion, Himalayan geodynamics, and the geomorphology of metamorphism, *GSA Today*, *11*(1), 4-9.

Zorin, Y. A., M. R. Novoselova, E. K. Turutanov, and V. M. Kozhevnikov (1990), Structure of the lithosphere of the Mongolian-Siberian mountainous province, *Journal of Geodynamics*, *11*(4), 327-342.

Zorin, Y. A. (1999), Geodynamics of the western part of the Mongolia-Okhotsk collisional belt, Trans-Baikal region (Russia) and Mongolia, *Tectonophysics*, *306*(1), 33-56.

FIGURE CAPTIONS

Figure 1: Regional map showing areas of high topography within Mongolia and southern Russia. The mean elevation in this view extent is 1500 ± 563 m and shows that the Hangay, Khövsgöl, Khentiyn, and Sayan Mountains (Russia) are a region of long-wavelength, high topography that has been dissected by the Selenga River network that drains the northern flank of the Hangay into Lake Baikal. Note that the deformation patterns vary regionally, i.e. the strong, large fault control in the Sayan versus the diffuse, smaller faults of the Hangay. The dark brown line denotes the 1500 m topographic contour. Regional fault systems are also shown; the sinistral Bulnai (BF) is the major strike-slip fault north of the Hangay separating the Sayan/Khövsgöl from the Hangay. The Mongolian (MA) and Gobi Altai (GA) ranges south of the Hangay are within a major transpressional fault system. The Siberian craton margin begins just north of the Sayan Mountains in the < 500 m elevation region (green) near the Mongolia-Russia border and Lake Baikal at ~53ºN latitude. Blue lines are major permanent streams draining higher elevations and the red line denotes the Selenga River system drainage divide. Heavy white line is Mongolian political border. Green dashed line is approximate Mongol-Okhotsk Ocean suture from *Van der Voo et al.* [2015]. Yellow star is Ulaanbaatar, the capital city. (MA=Mongolian Altai; GA=Gobi Altai; DL=Depression of Lakes; VL=Valley of Lakes; HM=Hangay Mountains; LK=Lake Khövsgöl; KM=Khentiyn Mountains; SM=Sayan Mountains; OR=Orkhon River; SR=Selenga River; LB=Lake Baikal; SB=Selenga basin). Major towns in Hangay region shown on figure 2.

Figure 2: The eastern Hangay Mountains and major rivers (blue lines) with high elevation areas glaciated in the LGM shown in gray. River incision estimates at locations (triangles) from basalt age data presented in *Ancuta* [2017]. Numbers shown are in incision rates in m/My. Circled area in the southeast is the headwaters of the Orkhon River. Gray triangle is the Orkhon waterfall location (Ulaan Tsutgalan). Photo on the right shows a canyon location along the Orkhon River, at lower elevations in the Selenga River basin, where the higher incision rates (~58 m/My) are due to local basalt flow damming (~180 m total thickness) over the past 3 m.y. Red dots mark major towns in the area. B = Bayankhongor; J = Jargalant; T = Tariat; Tg = Tsetserleg; Ts = Tosontsengal. Photo: The contact between granitic basement and the basalt flows is shown by the red line in the photo. Apatite (U-Th)/He sample 12MN09 is from the granite bedrock [mean (U-Th)/He age of ~325 Ma].

Figure 3: Imagery showing the regional topography near the highest Hangay peak, Otgontenger Uul (triangle). The areas outlined in white are the ELA for the LGM at 2800 m elevation. The image below is of the same area as above but showing elevations >2800 m (gray area is <2800 m) and areas with slopes ≤5° (orange). Enlarged digital elevation model (DEM) inset (top right, looking 240° at 20° inclination)

shows example of high elevation relict planation surface and associated cryoplanation features east of Otgontenger. Bottom panel is a slope map of another such area to the south with a flat, relict surface and cryoplanation terraces. See *West et al.,* [2013] for other examples.

Figure 4: **(A)** Hypsometry of the Selenga and Orkhon River sub-catchments sampled for detrital AHe (see figure 5 for locations; section 5 for discussion). **(B)** Schematic diagram illustrating the relationship between detrital thermochronometer data and the hypsometry of a catchment given an assumed positive age-elevation relationship where cooling ages should match the hypsometric curve if erosion is uniform, i.e. all points on the topography produce cooling ages that correspond to the basin AER. If there is non-uniform erosion, then the elevations on the landscape contributing sediments will affect the SPDF curve accordingly, modified after *Stock et al.* [2006].

Figure 5: Granitic-bedrock mean AHe ages across the Hangay Mountains and north-central Mongolia colored by age. The majority of cooling ages in the Hangay are ca. 100-120 Ma, with a slightly younger grouping <100 Ma on the north flank (red/white center). Off the Hangay, ages are similar, albeit with greater scatter and an older component greater than ca. 120 Ma. Detrital sample locations are shown as diamonds (mean age in italics). The red line shows the Selenga watershed and sub-catchments with respect to detrital samples for the Selenga and Orkhon are the orange lines. Points tagged in yellow are AHe/AFT transect (W) of *West et al.* [2013] shown in blue diamonds, transect (L) of *Landman* [2007] near Egiin Davaa, and transect (T) discussed with figures 7 and 8. OT = Otgontenger Uul. Grayscale 90 m DEM with 1700 m contour to mark higher elevations above the regional background and onset of 'regional knickpoint elevation zone' discussed in text and with fig. 7. Glaciated high elevations areas shown in cyan blue, derived from the ELA during the LGM from *Lehmkuhl* [1998]. Major faults from *Tomurtogoo* [1999] geologic map of Mongolia shown by heavy black lines. See supplement for full age dataset.

Figure 6: Selenga and Orkhon River detrital apatite (U-Th)/He cooling age populations shown by kernel density estimator (KDE) (smooth, gray envelope) and probability density functions (PDF) (shaded blue) from DensityPlotter [*Vermeesch*, 2012] using a Gaussian kernel and adaptive bandwidth (varied based on local data density). White dots show individual grain ages for the datasets. The y-axis is number of grains.

Figure 7: **(A)** Normalized CSPDF curves of Selenga detrital ages (dashed lines, t*) and catchment elevations (solid line, z*) for the Selenga River, using 95% and 99% of the detrital dataset, after *Ruhl and Hodges* [2005]. **(B)** SPDF curves for normalized age (gray) and elevation (solid black line) distributions with inset age and elevations (upper right). Dashed line in (B) is the 'ideal' age SPDF obtained from inverting the observed age SPDF and hypsometric curves with respect to the regional AER from the northern Hangay (figure 5, transect labelled T). Small inset panels show ages for 95% of the detrital AHe dataset and the elevations in the Selenga sub-catchment and red shading shows the dominant mismatch in age/elevation from the ideal age SPDF, see text for details.

Figure 8: Apatite AERs (left panel) from the western Hangay near Otgontenger (highest peak; figs. 3 and 4) incorporating a short transect from this study and from *West et al.* [2013] and *Landman* [2007] datasets (see fig. 5 for transect locations). Positive AERs suggest valley-scale topographic wavelengths do not affect low-T isotherms. Right panels show AFT and mean fission-track lengths (MTL) for *Jolivet et al.* [2007] and *West et al.* [2013] datasets. Planation surfaces in the Gobi Altai, Valley of Lakes, and W. Hangay (gray) are all similar in age suggesting regionally coincident exhumation and that highest elevations are preserved remnants from an older event. *West et al.* AFT transect suggests the period between ~180-130 Ma being governed by a moderate exhumation rate.

Figure 9: Pecube-NA sensitivity test of variables controlling relief to assess the ability to resolve relief change in this type of slow exhumation setting. For tests, a two-phase exhumation scenario was used with fixed rates of 100 m/My and 30 m/My. **(A)** Sensitivity test for *relief amplitude-only* showing least-squares misfit and relief amplitude between 0 (no relief) to 2 (two times modern relief) with a defined misfit minima at the true value of 0.5X the modern relief in the Hangay. **(B)** Misfit evolution over the sensitivity test inversion where τ, R, and E-timing are allowed free, exhibiting optimal convergence after >6000 models. **(C)** Correlation matrix for the free inversion parameters using NA-plot [*Sambridge*, 1999b]. Values approaching (-1)+1 show greater (anti)-correlation while values near 0 show no relationship or dependence. Erosional timescale and relief amplitude are highly anti-correlated, while both the exhumation rate change timing and relief amplitude have a slight positive correlation with erosional timescale. These trends can also be seen in the PPDFs in panels D to F. **(D-F)** Scatter plots showing misfit between τ, *R* and E-timing, the 2-D PPDF 1σ (solid) and 2σ (dashed) contours shown as overlays and the corresponding 1-D marginal PPDF curves for each parameter on the corresponding axes. In each case the star marks both the 'true parameter value' and in this case, the respective lowest misfit of the 1-D PPDF, which in this synthetic example is also the mean or modal value.

Figure 10: Pecube-NA inversion results for Run 1-TSW. Scatter plots are 2-D projections of the 5 dimensional parameter space on planes defined by combinations of two parameters. 1-D posterior curves show probability density within the parameter search range. See supplementary material for additional plots of other variables. Each dot represents a forward model from the inversion and is colored by the χ^2 misfit value. Stars denote the lowest misfit model while heavy/thin black lines are 1σ (67% confidence) and 2σ (95% confidence) errors, respectively. Bottom middle panel shows misfit evolution and convergence during the inversion and the bottom right shows the correlation matrix between difference parameters between -1 to +1 signifying strong (negative) anti-correlation or positive correlation, with values near zero having no relationship. Pecube physical modeling domain shown in fig. 13 inset box, see text for discussion.

Figure 11: Pecube-NA Run 1-C inversion results for 9504 models. The same figure scheme as figure 9. The difference between Run 1-TSW is that the exhumation rate change timing is allowed free in this inversion.

Figure 12: **(A)** Contoured age map (5 Ma interval) of Pecube-NA Run 1-TSW in the western Hangay (see fig. 13 for location, inset box). **(B)** Observed and predicted cooling ages and corresponding elevations are in good agreement except mainly at the highest elevations. Forward modeled using Pecube inversion modeled best-fit or maximum likelihood inversion values. Black circles are observed single-grain age replicates with errors, while squares are predicted cooling ages. **(C)** 1-to-1 line for predicted vs. observed cooling ages; gray squares are AFT samples. Vertical lines at age points correspond to the absolute difference between predicted ages that were better numerical fits to observed ages, and those that were not. **(D)** observed versus predicted elevations using best-fit 1-TSW inversion relief scenario in Pecube forward model.

Figure 13: Pecube forward model age predictions using inversion run 1-TSW best-fit parameter values with the main exhumation stage from 150-130 Ma after *West et al.* [2013] model thermal history. Inset box shows location of western Hangay bounds used in Pecube-NA inversion. Regional forward models are resampled at 10 km to smooth ages and are shown with a 5 Ma contour interval. (Top left) Elevations from 90m SRTM DEM (2000 m elev. contoured) with white dots showing sample locations used in Pecube modeling of the entire Hangay, (top right) the ages predicted by the best-fit model results of inversion 1-TSW shown in table 1 (Te = 6.1 km). Other panels show the effects of varying the effective elastic thickness (Te) while holding all other best-fit variables constant. Note the age scale change for the steady-state topography model.

Table 1: Fixed model parameters used in Pecube inversions to calculate the isostatic and thermal response to varying relief.

Table 2: Pecube-NA inversion results for sensitivity test and full inversions. Values separated by a colon are the prior search ranges during the NA sampling stage while those in bold are the best-fit parameter values (lowest misfit). Mean and standard deviation represent the resampling results from the NA appraisal of the model ensemble. *R* = relief amplitude; τ = erosional timescale; E-timing is the time of exhumation rate change; E_1 and E_2 = exhumation rate 1 and exhumation rate 2. See text for details.